

REPORT DOCUMENTATION PAGE

18

ing and
tion, including
A 22202-4302, and

* Public reporting burden for this collection of information is estimated to average 1 hour per response, including the maintaining the data needed, and completing and reviewing this collection of information. Send comments regarding suggestions for reducing this burden to Washington Headquarters Services, Directorate for Information Operations to the Office of Management and Budget, Paperwork Reduction Project (0704-0188), Washington, DC 20503.

0191

1. AGENCY USE ONLY (Leave blank)	2. REPORT DATE 5 July 1999	3. REPORT TYPE AND DATES COVERED Final 1 May 1995 - September 30 1998
4. TITLE AND SUBTITLE Epitaxial Metallic Compounds for Ideal Contacts to Compound Semiconductors		5. FUNDING NUMBERS G AF/F49620-95-1-0360
6. AUTHOR(S) Chris J. Palmstrøm Philip I. Cohen C. Barry Carter		
7. PERFORMING ORGANIZATION NAME(S) AND ADDRESS(ES) Regents of the University of Minnesota 1100 Washington Avenue South Minneapolis, MN 55415		8. PERFORMING ORGANIZATION REPORT NUMBER
9. SPONSORING / MONITORING AGENCY NAME(S) AND ADDRESS(ES) Air Force Office of Scientific Research Bolling AFB, DC 20332-6448		10. SPONSORING / MONITORING AGENCY REPORT NUMBER
11. SUPPLEMENTARY NOTES		
12a. DISTRIBUTION / AVAILABILITY STATEMENT PUBLIC DISTRIBUTION STATEMENT A Approved for Public Release Distribution Unlimited		12b. DISTRIBUTION CODE
13. ABSTRACT (Maximum 200 Words) Techniques for forming ideal contacts to compound semiconductors were developed. Atomic level structural characterization techniques, including scanning tunneling and transmission electron microscopy, as well as electrical characterization techniques were used to study the contact formation. By sequential depositions and reactions, metallic layers were first reacted with gallium arsenide to form a metal-gallium-arsenic compound. The consumption of gallium arsenide was controlled by the thickness of the metallic layer deposited. Sequential deposition of gallium or arsenic was used to drive the decomposition of the metal-gallium-arsenic compound, resulting in the solid phase regrowth of gallium arsenide beneath the metallic compound layer. The amount of regrown gallium arsenide could be controlled to atomic length scales by the supply of gallium or arsenic. Magnetization controlled resonant tunneling through buried semi-metallic quantum wells was demonstrated. Further aluminum arsenide was used to terminate gallium arsenide so that atomically abrupt iron aluminum could be grown. Iron aluminum compounds were found to have different growth modes, which correlated with the surface reconstruction. The properties of the films were measured. Finally, GaN films were grown on sapphire and then hafnium and hafnium nitride epitaxial films were grown. Hafnium growth on gallium nitride proceeded via a hafnium nitride interlayer.		
14. SUBJECT TERMS Epitaxy, contacts, semiconductors, metallizations, gallium nitride, gallium arsenide		15. NUMBER OF PAGES 58
		16. PRICE CODE
17. SECURITY CLASSIFICATION OF REPORT Unclassified	18. SECURITY CLASSIFICATION OF THIS PAGE Unclassified	19. SECURITY CLASSIFICATION OF ABSTRACT Unclassified
20. LIMITATION OF ABSTRACT		

NSN 7540-01-280-5500

Standard Form 298 (Rev. 2-89)
Prescribed by ANSI Std. Z39-18
298-102

Final Report: Epitaxial Metallic Compounds for Ideal Contacts to Compound Semiconductors (AF/F49620-95-1-0360)

Christopher J. Palmstrøm*, Philip I. Cohen[†] and C. Barry Carter*

*Chemical Engineering and Materials Science

[†]Electrical and Computer Engineering

University of Minnesota

Minneapolis, MN 55455

1 Executive Summary

During the early part of this grant, significant effort was dedicated to establishing Palmstrøm's research facility after his move from Bellcore. This involved assembling and installing two molecular beam epitaxy (MBE) machines, which had been purchased with University startup funds. In addition scanning tunneling microscopy (STM) capability was added to the MBE machines in Cohen's laboratory. During this initial phase collaborative research programs were established with L.C. Wang at Texas A&M on solid phase regrowth ohmic contacts and the operational gas source molecular beam epitaxy systems in Cohen's laboratory enabled studies on improving the growth of GaN and growing epitaxial metallic layers on GaN. In addition, extensive collaborations were established with Jim Allen at UCSB. After the two molecular beam epitaxy machines and STM became fully operational, research projects involving epitaxial growth of thermodynamically stable metallic compounds on GaAs and GaAlAs semiconductors, semiconductor overgrowth on metallic compounds, magnetization controlled resonant tunneling through buried metallic compound layers, controlling metal semiconductor reactions and semiconductor regrowth, and controlling growth of GaN were established. An in-situ electrical probe station attached to a molecular beam epitaxy system was developed. It enabled the reaction kinetics at metal/semiconductor interfaces to be determined electrically without removing the sample from the ultra high vacuum system. In situ control of the GaN films enabled studies on high quality GaN surfaces. Using the STM atomic resolution studies of metal overgrowth of GaN was performed. Arsenic capped films were transferred from the MBE machines in Palmstrøm's laboratory to the STM in Cohen's laboratory. Cross sectional transmission electron microscopy of samples was performed by Carter's group.

Most significant advancements and conclusions

- Demonstrated how the knowledge of thermodynamics and reaction kinetics can be used to control interfacial reactions in metal/semiconductor systems at the nm level.
- Demonstrated controlled reaction penetration depth of a metal into a compound semiconductor followed by controlled regrowth of the semiconductor by inducing a second reaction through sequential controlled deposition and reaction.
- Solid Phase Regrown GaAs at ~300°C shows good electronic properties.
- Contact formed using the solid phase regrowth process induced by arsenic are good Schottky barrier contacts.
- Developed in-situ shadow mask technology for diode fabrication.
- Designed and implemented an in-situ electrical probe station for device characterization using current-voltage and capacitance-voltage measurements.

19990818 270

- In-situ electrical measurements were used to measure motion of the contact/semiconductor interface as a result of metal/semiconductor reactions and subsequent solid phase regrowth for individual diodes.
- Demonstrated growth of high quality $\text{Fe}_{1-x}\text{Al}_x$ epitaxial films on AlAs.
- First demonstration that growth mode could be correlated with ordered superlattice structure.
- Correlation of surface morphology of FeAl with surface reconstruction.
- Atomic resolution Scanning Tunneling Microscopy (STM) was achieved on epitaxial metallic compounds grown on $\text{Ga}_{1-x}\text{Al}_x\text{As}$ surfaces.
- As-capping and transfer in air followed by decapping was found to be an effective technique for transferring rare-earth monoarsenide samples fabricated in one system to the STM of another.
- Developed GaN surfaces suitable as substrates for metallic epitaxial overlayers.
- Developed the first realistic growth model of GaN.
- Showed that Ga accumulation on GaN inhibited decomposition of ammonia.
- First to grow epitaxial HfN on GaN(0001).
- Showed that Hf growth on GaN proceeds via a HfN interlayer.
- Applied interlayers for improving the overgrowth of compound semiconductors on epitaxial thermodynamically stable metallic compounds and developed a bond angle tailoring model interpreting the mechanism of improving the interfacial bonding.
- Demonstrated magnetic field controlled resonant tunneling through buried semi-metallic ErAs layers (in collaboration with Jim Allen at UCSB).

1.1 People Involved with Research

PI's: C.J. Palmstrøm, P.I. Cohen, and C.B. Carter

Postdocs: A. Bensaoula, A.M. Dabiran

Visiting Scientist: T.G. Finstad

Graduate Students: D. Caldwell, L.-C. Chen, B. Ishaug, J. Farrer, D. Cohen, E. Linville,

A. Parkhomovsky, R. Held, A.M. Johnston, D.E. Crawford, S.M. Seutter, and J.W. Dong

Undergraduate Student: W. Schildgen

1.2 Theses Generated

Master Thesis:

Douglas A. Caldwell "Regrowth of GaAs Through Controlled Solid Phase Thin Film Reactions", October, 1998

Brian Ishaug, "Magnetic Properties, Nucleation, and Growth of FeAl on AlAs/GaAs," Jan 1998, M.S.E.E.

1.3 Publications Resulting from this Proposal:

- 1 L. C. Chen, D. A. Caldwell, T. A. Müller, T. G. Finstad, W. Schildgen and C. J. Palmstrøm, "MBE growth and in-situ electrical characterization of metal/semiconductor structures", *J. Crystal Growth*, **201/202**, 146 (1999)
- 2 L. C. Chen and C. J. Palmstrøm, "In-situ electrical determination of reaction kinetics and interface properties at MBE-grown metal/semiconductor interfaces", *J. Vac. Sci. Technol. B*, accepted (1999)

3 L. C. Chen, D. A. Caldwell, T. G. Finstad and C. J. Palmstrøm, "In-situ formation, reactions, and electrical characterization of MBE-grown metal/semiconductor interfaces", *J. Vac. Sci. Technol. A*, accepted (1999)

4 A. Parkhomovsky, B. E. Ishaug, A. M. Dabiran and P. I. Cohen, "Growth of Hf and HfN on GaN by molecular beam epitaxy", *J. Vac. Sci. Technol.*, in press (1999)

5 D. A. Caldwell, L. C. Chen, A. H. Bensaoula, J. K. Farrer, C. B. Carter and C. J. Palmstrøm, "In-situ controlled reactions and phase formation of thin films on GaAs", *J. Vac. Sci. Technol. B*, **16**, 2280 (1998)

6 D. A. Caldwell, L.-C. Chen, A. H. Bensaoula, J. K. Farrer, C. B. Carter and C. J. Palmstrøm, "In-situ regrowth of GaAs through controlled phase transformations and reactions of thin films on GaAs", *Proc. Mat. Res. Soc. Symp.*, **514**, 455 (1998)

7 J. K. Farrer, D. A. Caldwell, C. J. Palmstrøm and C. B. Carter, "Solid-phase epitaxial regrowth of GaAs by in-situ controlled intermediate phase decomposition", *EMSA*, (1998)

8 B. E. Ishaug, S. M. Seutter, A. M. Dabiran, P. I. Cohen, R. F. C. Farrow, D. Weller and S. S. P. Parkin, "Nucleation, growth and magnetic properties of epitaxial FeAl films on AlAs/GaAs", *Surface Science*, **380**, 75 (1997)

9 D. R. Schmidt, J. P. Ibbetson, D. E. Brehmer, C. J. Palmstrøm and S. J. Allen, "Giant magnetoresistance of self-assembled ErAs islands in GaAs", *Mat. Res. Soc. Symp. Proc.*, **475**, 251 (1997)

10 M.-H. Park, L. C. Wang and C. J. Palmstrøm, "Low resistance Pd/Zn/Pd ohmic contacts to p-Ga_{0.82}In_{0.18}As_{0.39}P_{0.61}", *J. Appl. Phys.*, **81**, 2720 (1997)

11 M.-H. Park, L. C. Wang, J. Y. Cheng and C. J. Palmstrøm, "Low resistance ohmic contact scheme ($\sim \mu\Omega \text{ cm}^2$) to p-InP", *Appl. Phys. Lett.*, **70**, 99 (1997)

12 D. E. Crawford, R. Held, A. M. Johnston, A. M. Dabiran and P. I. Cohen, "Growth rate reduction of GaN due to Ga surface accumulation", *MRS Internet J. Nitride Semiconductor Research*, **1**, Article 12 (1996)

13 D. E. Brehmer, Z. Kai, C. J. Schwarz, S. P. Chau, S. J. Allen, J. P. Ibbetson, J. P. Zhang, A. G. Petukhov, C. J. Palmstrøm and B. Wilkens, "Resonant tunneling through rare earth arsenide, semimetal quantum wells", *Solid-State Electron. (UK)*, **40**, 241 (1996)

14 P. F. Miceli, J. Weatherwax, T. Krentsel and C. J. Palmstrøm, "Specular and diffuse reflectivity from thin films containing misfit dislocations", *Physica B*, **221**, 230 (1996)

15 M.-H. Park, L. C. Wang, J. Y. Cheng, F. Deng, S. S. Lau and C. J. Palmstrøm, "Low resistance Zn₃P₂/InP heterostructure ohmic contact to p-InP", *Appl. Phys. Lett.*, **68**, 952 (1996)

16 C. J. Palmstrøm, "Epitaxy of dissimilar materials", *Annu. Rev. Mater. Sci.*, **25**, 389 (1995)

17 D. E. Brehmer, K. Zhang, C. J. Schwarz, S.-P. Chau, S. J. Allen, J. P. Ibbetson, J. P. Zhang, C. J. Palmstrøm and B. J. Wilkens, "Resonant tunneling through ErAs semimetal quantum wells", *Appl. Phys. Lett.*, **67**, 1268 (1995)

2 Table of Content

1	Executive Summary.....	i
1.1	People Involved with Research	ii
1.2	Theses Generated.....	ii
1.3	Publications Resulting from this Proposal:.....	ii
2	Table of Content.....	iv
3	Control of Metal/Semiconductor Interfacial Reactions.....	1
3.1	Background	1
3.2	Approach	2
3.3	Experimental Procedure.....	3
3.3.1	Reaction (1): Ni/GaAs.....	4
3.3.2	Reaction (2): As ₄ reactions with Ni ₃ GaAs/GaAs	7
3.3.3	Reaction (3): Ga reactions with Ni ₃ GaAs/GaAs.....	10
3.3.4	In-situ Electrical Measurements	11
3.3.5	Schottky barrier height and Ideality Factor Measurements.....	13
3.3.6	Doping depth profiles.....	16
4	Nucleation and Growth and Properties of Epitaxial Fe _x Al _{1-x} films	23
4.1	Introduction	23
4.2	Experimental	25
4.3	Results and Discussion.....	25
4.3.1	Nucleation.....	25
4.3.2	Annealing	27
4.3.3	Growth.....	29
4.3.4	Magnetic Properties	29
4.4	Conclusion.....	31
5	Growth of Hf and HfN on GaN by Molecular Beam Epitaxy	32
5.1	Introduction	32
5.2	Experimental	32
5.3	Results.....	33
5.4	Discussion	35
5.5	Summary	37
6	Atomic Level Characterization of Epitaxial Grown Metallic Compounds on III-V Semiconductors.....	37
7	Semiconductor Growth on Metallic Compound Layers.....	38
7.1	Controlling Semiconductor Overgrowth Through the use of a Bond Tailoring Interlayer (interface energy modification).....	39
8	Magnetotransport in Metallic Compound/Semiconductor Heterostructures	41
9	Growth Rate Reduction of GaN Due to Ga Surface Accumulation.....	43
9.1	Introduction	43
9.2	Experimental	43
9.3	Results.....	44
9.3.1	Transient Response of the Surface Composition.....	44
9.3.2	Steady State Growth Behavior.....	46
9.4	Conclusions	50
10	References	51

3 Control of Metal/Semiconductor Interfacial Reactions

In order to obtain ideal contacts to compound semiconductors, the thermodynamics of metal/semiconductor reactions must be completely understood. In the past, reactions of metals with semiconductors have been studied in order to investigate reaction kinetics and phase formation without attempts for controlling the phase formation[1-4]. **The objective of this study was to determine to what degree interfacial reactions can be controlled and the relevance of bulk ternary phase diagrams to thin film reactions.**

3.1 Background

In earlier studies, we have shown that the Ni/GaAs reaction starts at annealing temperatures of less than 200°C and is very rapid above 200°C[5]. The reaction follows equation (1) and results in the formation of Ni_xGaAs at the Ni/GaAs interface, where x ranges from 2 to 4[5-8].



Ni_xGaAs is thermodynamically stable. However, it is not thermodynamically stable in contact with GaAs.

Figure 1 shows an isothermal section of the ternary Ni-Ga-As phase diagram formed by combining ones reported in the literature[9-11]. The lack of a tie line between Ni_xGaAs and GaAs indicates the lack of thermodynamic stability for Ni_xGaAs in contact with GaAs. Ni_xGaAs is expected, as has been observed for anneals >400°C, to decompose into NiGa and NiAs[3,7,12,13], which are stable phase in contact with GaAs[3,14,15]. Although, the Ni-Ga-As system is one of the most studied M-Ga-As ternary phase diagrams[9-11], it is still controversial[16,17]. The group at the University of Wisconsin report that a single Ni_xGaAs ternary phase with a very large phase field (unshaded outlined region) extends from NiAs through the multiple individual phases A, B (Ni_3GaAs), D ($\text{Ni}_{3.6}\text{GaAs}$) and E reported by Guérin et al.[16] shown in Fig. 1. Note that only phases B and D can have equal amounts of Ga and As, whereas A, C and E must be either Ga- or As-rich. We will show that neither ternary phase diagram is completely consistent with our results.

The ternary phase diagram also indicates that Ni_2Ga_3 is stable in contact with GaAs. The fact that NiAs_2 was not observed in the experimental verification of the ternary phase diagram suggests that NiAs_2 itself is not stable at the temperatures and pressures used in these studies.

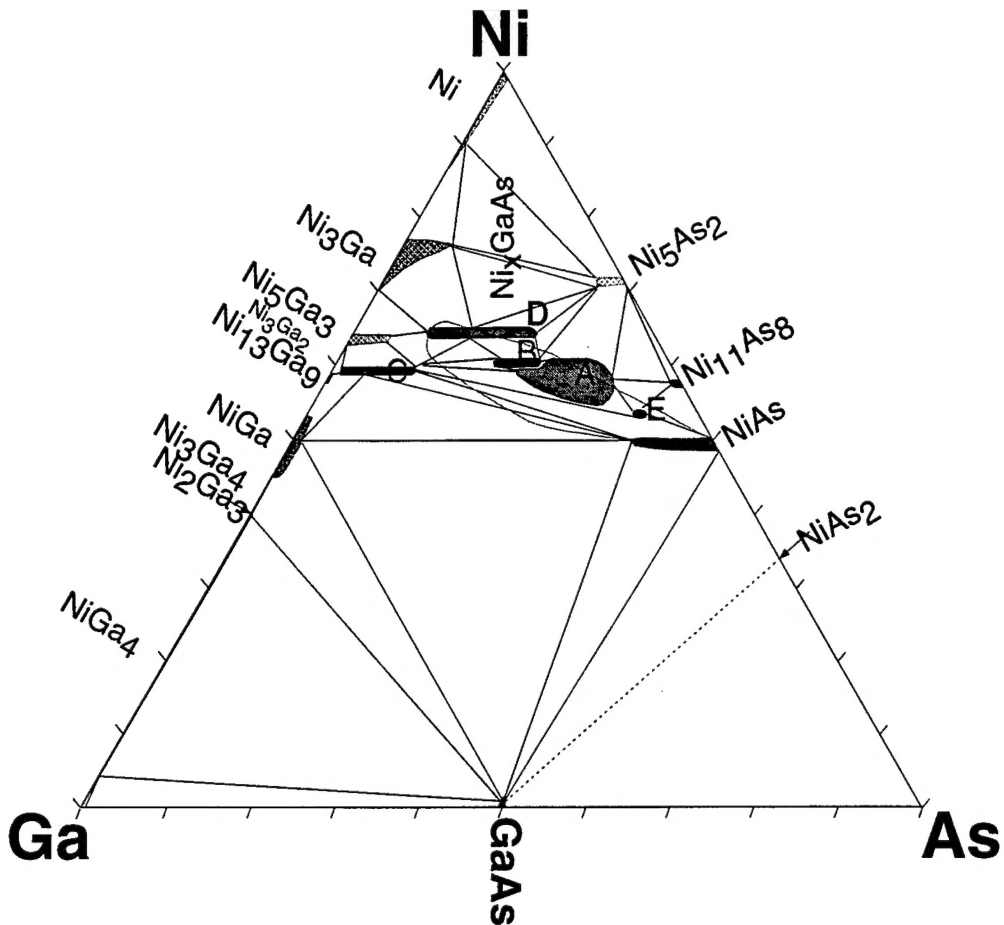


Fig. 1 Isothermal section of the Ni-Ga-As constructed from data in references [9-11]

3.2 Approach

From the phase diagram in Fig. 1, we predicted that $\text{Ni}_x\text{GaAs}/\text{GaAs}$ would decompose to NiAs and GaAs if exposed to an arsenic flux through reaction (2), and to NiGa or Ni_2Ga_3 and GaAs if exposed to a Ga flux (reactions 3a and 3b, respectively). We found that the Ni_2Ga_3 formed.



Furthermore, we predicted further that the GaAs formed through reactions (2) and (3) would regrow epitaxially on the GaAs substrate by solid phase regrowth in a similar manner to that observed in reactions of bilayer structures deposited on GaAs such as $\text{Si}/\text{Ni}/\text{GaAs}$ [18], $\text{Si}/\text{Pd}/\text{GaAs}$ [19] and $\text{Al}/\text{Ni}/\text{GaAs}$ [20].

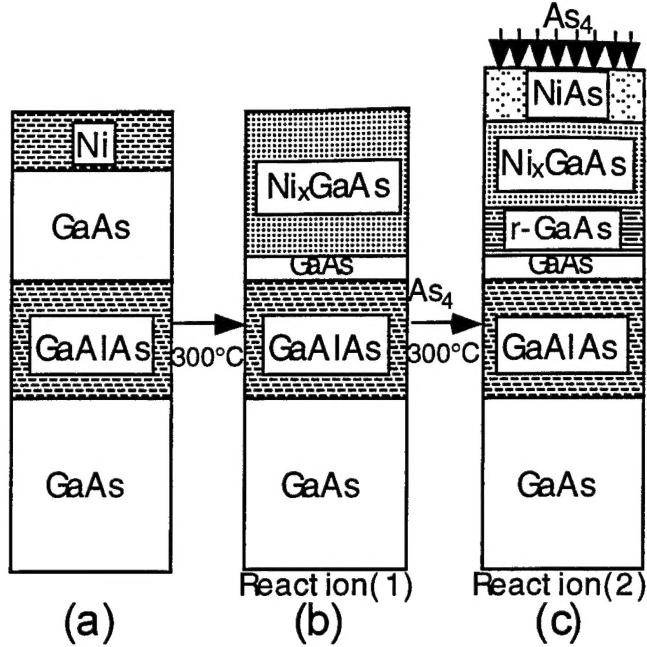


Fig. 2 Schematic of the sequential reaction procedure used for a Ni/GaAs/Ga_{0.5}Al_{0.5}As/GaAs structure: (a) as-deposited, (b) reaction (1) induced by 300°C annealing, and (c) reaction (2) induced by As₄ exposure at 300°C.

We predicted further that the penetration depth would be controlled by the amount of Ni deposited through completion of reaction (1), as shown in Fig. 2(a) and (b) and that the thickness of regrown GaAs could be controlled by the amount of As or Ga supplied for reaction (2) and (3), respectively.

3.3 Experimental Procedure

n⁺-doped GaAs (100) substrates were In bonded to Mo sample blocks and loaded into a modified VG Semicon V80H molecular beam epitaxy (MBE) system with a base pressure of $\sim 5 \times 10^{-11}$ mbar. For each substrate, after native oxide removal and annealing at 640°C under an As₄ overpressure, a GaAs buffer layer was grown at 580°C. For structural measurements an additional 1000Å thick Ga_{0.5}Al_{0.5}As marker layer was grown at a depth of 1000Å from the GaAs surface. The as-grown structures were annealed at 580°C for 10 min in the growth chamber under an As₄ flux to form a smooth surface, then it was cooled until the sample temperature reached 350°C, at which point the As₄ flux was shut off. This process results in the formation of an As-rich c(4×4) surface reconstruction on the as-grown GaAs surface. The samples were transported in ultra high vacuum (UHV) to an integral chamber with electron beam evaporation sources for Ni deposition. After Ni deposition, the samples were transported back to the MBE growth chamber under UHV for subsequent annealing and reactions. This enabled reflection high-energy diffraction (RHEED) studies to be performed during the annealing and reactions. A constant heater output power was used in order to ensure no temperature overshoot during the annealing. This resulted in a slow ramp rate. The annealing took place at a growth chamber pressure of $< 2 \times 10^{-10}$ mbar for 10 min at 300°C prior to As₄ exposure. The As₄ flux used to induce reaction (2) was supplied from a valved cracking

effusion cell. The use of a valved cracker allowed for controlled As_4 exposure times with negligible background As_4 pressure in the chamber. As-RHEED oscillations observed from As_4 -induced GaAs growth from predeposited Ga on GaAs were used to determine the As_4 flux. The flux resulted in a GaAs growth rate of ~2 bilayers/s at 580°C which corresponds to an effective As incorporation flux of $\sim 1.2 \times 10^{15} \text{ As atoms cm}^{-2} \text{ s}^{-1}$. A conventional effusion cell was used for Ga induced regrowth (Reaction (3)).

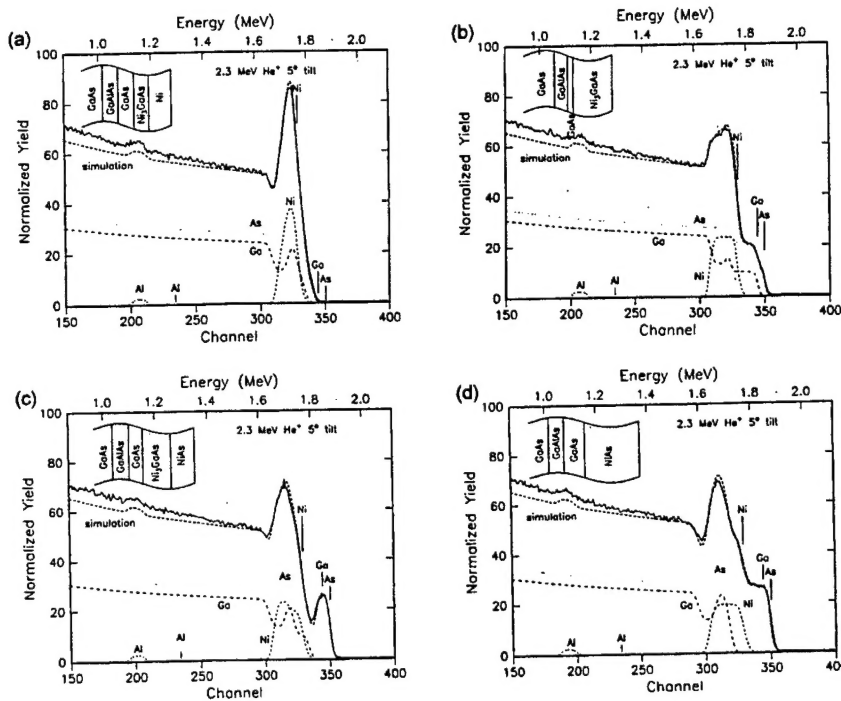


Fig. 3 RBS spectra of $\text{Ni}/\text{GaAs}/\text{Ga}_{0.5}\text{Al}_{0.5}\text{As}/\text{GaAs}$ structures: (a) as-deposited, and annealed at 300°C for 10 min followed by As_4 exposure times of (b) 0, (c) 3, and (d) 10 min. The simulated spectra (dashed lines) and deconvolutions of the simulated spectra indicating the contribution from each element are also shown.

3.3.1 Reaction (1): Ni/GaAs

After deposition a streaky RHEED pattern was observed from the Ni films with the electron beam incident along $<010>$ direction of GaAs, indicating a highly oriented or epitaxial Ni film. The streaky RHEED pattern started disappearing at 240°C while heating the Ni/GaAs structure from room temperature to 300°C . A ringed polycrystalline pattern appeared at 245°C and finally another streaky pattern appeared between 250 and 260°C . This pattern did not change upon further annealing at 300°C for over 30 min.

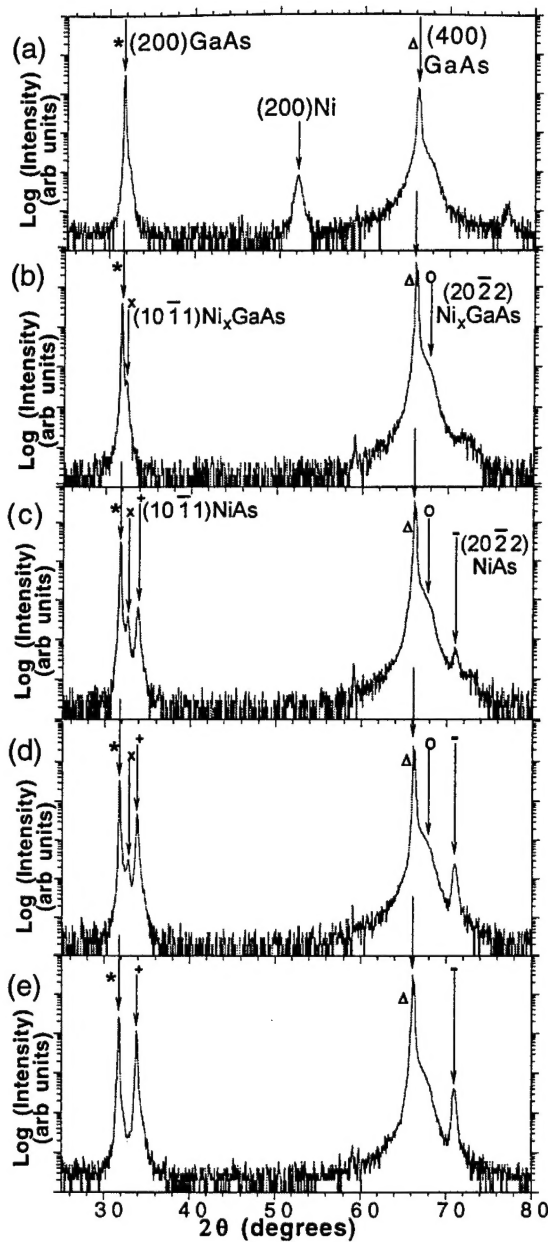


Fig. 4 X-ray diffraction spectra of Ni/GaAs/Ga_{0.5}Al_{0.5}As/GaAs structures: (a) as-deposited and annealed at 300°C for 10 min followed by As₄ exposure times of (b) 0, (c) 1, (d) 3, and (e) 10 min.. (a) shows a (200)Ni peak in addition to (200)GaAs (*) and (400)GaAs (Δ) peaks. Annealing results in Ni_xAs (x = (1011) and o = (2022)) formation and with subsequent As₄ exposure the Ni_xAs peak intensities decrease and the NiAs (+ = (1011) and - = (2022)) increase.

Fig. 3 shows the RBS spectra from as-deposited, annealed and reacted samples. The RBS spectra in Fig. 3(a) and (b) correspond to the as-deposited and 300°C annealed Ni/GaAs structures, respectively. There is a dramatic difference between the two spectra. The insert in each figure corresponds to the structure used for the simulation of the RBS spectrum. The simulated spectra have been deconvoluted to show the contributions from each element. The dip in the simulated Ga signal at about channel 310 corresponds to the Ga signal from the $\text{Ga}_{0.5}\text{Al}_{0.5}\text{As}$ layer and the peak in the simulated Ga signal at about channel 325 corresponds to the Ga signal from the GaAs layer on top of the $\text{Ga}_{0.5}\text{Al}_{0.5}\text{As}$. An excellent fit to the as-deposited sample spectrum (Fig. 3(a)) was achieved with a thin layer of Ni_3GaAs between the Ni and GaAs. This reacted layer may have formed during the Ni deposition or more likely during the heating ($>160^\circ\text{C}$) required to melt the In during sample removal from the Mo sample holder. The spectrum in Fig 3(b) shows that the Ni has completely reacted with the GaAs to form Ni_3GaAs during the *in-situ* 300°C 10 min anneal. The GaAs layer beneath this reacted layer is clearly much thinner as is evident from the reduced simulated Ga signal in the peak at about channel 325. Results from x-ray diffraction studies confirm the interpretation of the RBS data.

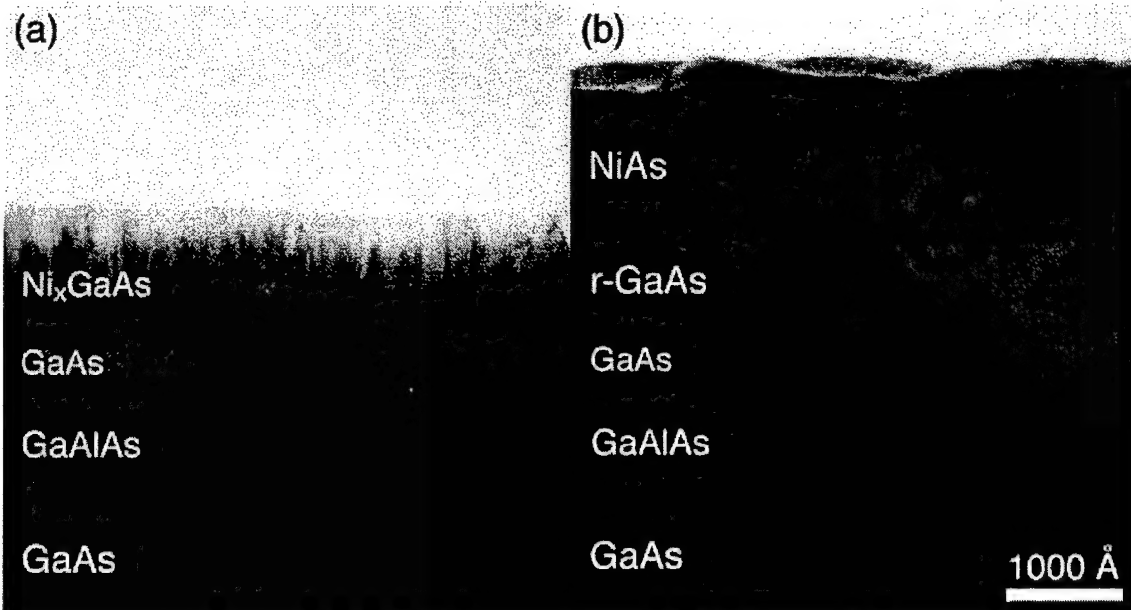


Fig. 5 Cross-sectional TEM micrographs of Ni/GaAs/ $\text{Ga}_{0.5}\text{Al}_{0.5}\text{As}/\text{GaAs}$ structures annealed to 300°C for 10 min (a) without subsequent As_4 exposure and (b) with 10 min of subsequent As_4 exposure at 300°C. (The rough $\text{GaAs}/\text{Ga}_{0.5}\text{Al}_{0.5}\text{As}$ interface is a result of a rough $\text{Ga}_{0.5}\text{Al}_{0.5}\text{As}$ surface during MBE growth of this layer).

Fig. 4 shows the x-ray diffraction patterns obtained from the as-deposited, annealed and reacted samples. For the as-deposited sample the (200) Ni and the (200) and (400) GaAs substrate peaks are observed (Fig. 4(a)). This indicates that the Ni grows with a preferred orientation of (100) Ni || (100) GaAs, which is consistent with the

RHEED data. The diffraction pattern from the 300°C annealed sample (Fig. 4(b)) shows peaks corresponding to (10 $\bar{1}$ 1) and (20 $\bar{2}$ 2) Ni_xGaAs in addition to the substrate peaks. No elemental Ni peaks are observed, indicating complete Ni_xGaAs formation. A cross-sectional TEM micrograph of the annealed sample is shown in Fig. 5(a). It shows a fine vertical-grained Ni₃GaAs layer ~1000Å thick above a thin (~300Å) unreacted GaAs layer over the ~1000Å thick Ga_{0.5}Al_{0.5}As marker layer. The selected area diffraction pattern from the Ni₃GaAs corresponds to diffraction patterns obtained along the <2 $\bar{1}\bar{1}0$ > zone axis of two variants. The observed orientation relationship (10 $\bar{1}$ 1)<2 $\bar{1}\bar{1}0$ > Ni₃GaAs || (100)<011> GaAs is consistent with that reported by Sands et al.[6].

Simulations of the RBS spectra in Fig. 3 indicate a value of 3 for x. The Ni_xGaAs lattice parameters as a function of x have been reported by Chen et al. using electron diffraction[8]. Their data would correspond to $d_{(10\bar{1}1)}=2.75\text{\AA}$ when x=2.5 and $d_{(10\bar{1}1)}=2.81\text{\AA}$ when x=4. Assuming a linear interpolation, the value of $d_{(10\bar{1}1)}=2.77\text{\AA}$ determined from the x-ray diffraction data in Fig. 4(b) would also be consistent with an x value of 3. The lattice parameters of $a=3.835\text{\AA}$ and $c=5.032\text{\AA}$ ($c/a=1.31$) were determined from TEM selective area diffraction patterns and are consistent with the X-ray diffraction data. These data are in excellent agreement with the values reported by Lahav et al.[7] ($a=3.83\text{\AA}$, $c=5.04\text{\AA}$, $c/a=1.316$) for a 300°C annealed sample, which was reported to have a composition of Ni₂GaAs. A detailed study of the many different Ni_xGaAs phases has been made by Guérin and Guivarc'h[9]. The lattice parameters reported here are intermediate between the Guérin and Guivarc'h[9] reported values for the B and A Ni_xGaAs phases (see Fig. 2), which both have x values close to 3. However, the A phase is always As-rich and does not extend to an equal Ga to As ratio (see Fig. 1). Sands et al.[6] have measured the lattice parameters of Ni_xGaAs formed by thin film reactions as a function of annealing conditions. The composition of Ni_xGaAs can also be determined from the micrograph in Fig. 5(a). 500Å of Ni (4.6×10^{17} atoms/cm²) would consume 690Å (3.05×10^{17} atoms/cm²) GaAs to form Ni₃GaAs. As the initial GaAs layer was 1000Å thick, this would leave 310Å unreacted GaAs, as is observed in the micrograph. These results together with the regrowth results below suggest that the Ga to As ratio is unity, which suggests that the A-phase extends all the way to equal Ga to As ratio.

Based on the changes in the RHEED patterns during the annealing, it appeared that the Ni/GaAs reaction (reaction (1)) proceeded rapidly at temperatures $\leq 250^\circ\text{C}$ and was completed before the sample reached 300°C. This is consistent with the reported Ni/GaAs reaction kinetics[8]. Ni has been reported to be the dominant diffusing species[7,8,21]. Palmström et al.[22] pointed out in the Co/GaAs system that Co₂GaAs formation results from Co indiffusion into the GaAs and that CoAs and CoGa can only form when there is diffusion of Ga and As. The formation of Ni₃GaAs without NiGa or NiAs formation results from Ni indiffusion into the GaAs with Ga and As being essentially immobile. This explains why Ni₃GaAs is formed at these low temperatures rather than NiGa and NiAs, which the Ni-Ga-As ternary phase diagram predicts.

3.3.2 Reaction (2): As₄ reactions with Ni₃GaAs/GaAs

Reaction (2) was induced by exposing the $\text{Ni}_3\text{GaAs}/\text{GaAs}$ structure formed by reaction (1) to an As_4 flux while the sample was held at 300°C . With the electron beam incident along the $\text{GaAs} <010>$, the streaky RHEED pattern from the Ni_3GaAs changed abruptly to a more spotty pattern, indicating diffraction from a rough surface. The diffraction pattern kept changing during the As_4 exposure. Within 1 min of exposure, the RHEED pattern became more streaky and after 2 min additional faint streaks, possibly due to a $3\times$ surface reconstruction, were observed. After 6.5 min, the RHEED pattern consisted of streaks with chevrons, indicating a faceted surface. Further exposure to As_4 did not result in a change in the RHEED pattern. This indicates that reaction (2) was completed after 6.5 min of As_4 exposure.

The Ni_xGaAs x-ray diffraction peaks decrease and the NiAs peaks increase with As_4 exposure (Fig. 4). Fig. 4(e) has no diffraction peaks for Ni_3GaAs , showing that reaction (2) is complete after 10 min of As_4 exposure. These x-ray diffraction data also show that NiAs grows with the same perpendicular orientation as Ni_3GaAs , i.e. $(10\bar{1}1)$ $\text{NiAs} \parallel (100)$ GaAs . Further, the lattice parameters of the Ni_3GaAs change slightly with As_4 exposure, $d_{(10\bar{1}1)} = 2.750\text{\AA}$ and 2.737\AA after 1 min and 3 min exposure, respectively, indicating a possible change in composition. However, as GaAs regrowth is observed, compositional variation in the Ni_3GaAs is unlikely to involve significant changes in the Ga to As ratio, but may involve a change in the Ni content of the Ni_3GaAs . This suggests that there must be a larger phase field for Ni_xGaAs than phases D and B would suggest. We speculate that phase A also extends further into the a region of equal Ga and As concentration. The ternary phase diagram was obtained at high temperature ($\sim 600^\circ\text{C}$) and at the lower reaction temperatures used here, it is likely that the phase fields will be larger.

Figs. 3(c) and (d) show the RBS spectra obtained for $\text{Ni}_3\text{GaAs}/\text{GaAs}$ structures after exposure to a constant As_4 flux for 3 min and 10 min, respectively. Fig. 3(c) clearly shows that NiAs forms on the Ni_3GaAs surface and that GaAs regrows at the $\text{Ni}_3\text{GaAs}/\text{GaAs}$ interface. This is evident from the deconvoluted simulated spectrum. The large peak at about channel 345 is due to the As in the NiAs surface layer and the peak in the Ga simulated signal at channel 320 is due to the GaAs layer on top of the $\text{Ga}_{0.5}\text{Al}_{0.5}\text{As}$. The fact that this peak is larger than that observed for the $\text{Ni}_3\text{GaAs}/\text{GaAs}$ structure prior to As_4 exposure demonstrates that regrowth of GaAs has occurred. Comparing the size and position of this Ga peak in Figs. 2(b), (c) and (d) indicates that it grows in size and moves to lower energy (channel number) as a result of As_4 exposure. The Al peak can also be seen to move to lower energy as a result of the As_4 exposure. The increase in size of the Ga peak corresponds to an increase in the thickness of the GaAs layer on top of the $\text{Ga}_{0.5}\text{Al}_{0.5}\text{As}$ (i.e. GaAs regrowth). The shift in energy of the Ga and Al peaks results from the increase in thickness of material above the GaAs layer due to the incorporation of As from the As_4 flux into the NiAs layer at the surface. The simulated spectrum for Fig. 2(d) corresponds to the completion of reaction (2) with the formation of a $\text{NiAs}/\text{GaAs}/\text{Ga}_{0.5}\text{Al}_{0.5}\text{As}/\text{GaAs}$ structure, which is confirmed by the cross-sectional TEM of the same sample shown in Fig. 5(b). The layered structure of $\text{NiAs}/\text{regrown GaAs}/\text{GaAs}/\text{Ga}_{0.5}\text{Al}_{0.5}\text{As}/\text{GaAs}$ can easily be seen. The grain structures of Ni_3GaAs and NiAs are distinctly different with grains of NiAs being much larger and less elongated (Fig. 4). The regrown GaAs layer is epitaxial. However, it has some inclusions and stacking faults. The inclusions are probably NiAs . NiAs precipitates have been reported to form in GaAs regrown using $\text{Si}/\text{Ni}/\text{GaAs}$ structures[18]. The stacking faults are likely to have nucleated on inclusion. The rough $\text{GaAs}/\text{Ga}_{0.5}\text{Al}_{0.5}\text{As}$ interface is a result of a rough $\text{Ga}_{0.5}\text{Al}_{0.5}\text{As}$ surface during the MBE growth of this layer.

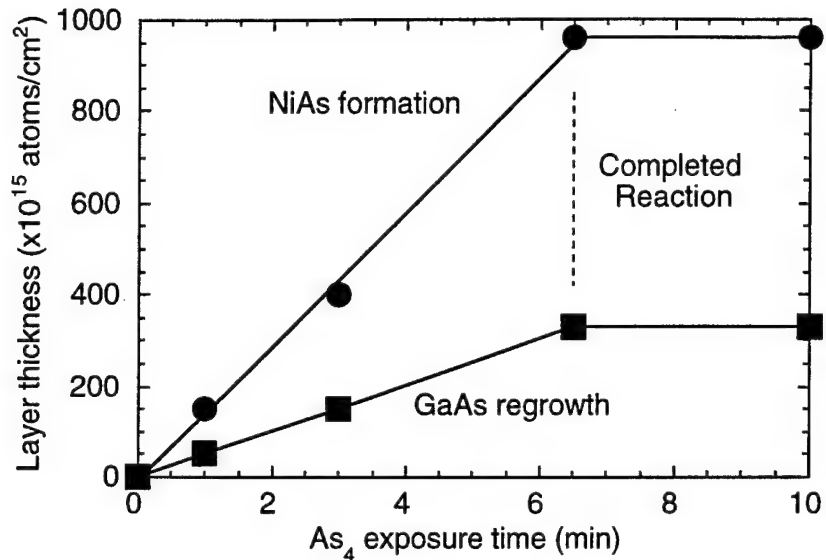


Fig. 6. Plot of thickness of reaction products as a function of As₄ exposure time at 300°C for Ni_xGaAs/GaAs structures. A linear relationship is found between thickness and exposure time, implying that reaction (2) is limited by arrival of As₄ at the sample surface.

The reaction rate for the NiAs formation and the GaAs regrowth can be determined from RBS data. Fig. 6 shows a plot of the NiAs and regrown GaAs thicknesses (in atoms/cm²) as a function of the As₄ exposure time. A linear increase in both the NiAs and GaAs is observed up to 6.5 min exposure, after which no further increase is observed. No further increase results from reaction (2) being completed as no further Ni is available for NiAs formation. The linear dependence on time indicates reaction limited growth. A fit to the NiAs linear growth rate corresponds to an As incorporation rate of 1.2×10^{15} atoms•cm⁻²•s⁻¹, which is in excellent agreement with the As incorporation flux measured by As-induced RHEED oscillations during GaAs growth. This demonstrates that the arrival rate of As is the limiting factor in the reaction rate. The detailed mechanism involved in the reaction is not known. Either the Ni is diffusing out from the Ni₃GaAs, resulting in GaAs regrowth or As is diffusing in and displacing the GaAs. Chen et al[8] estimated the Ni interdiffusion coefficient in Ni_xGaAs from lateral Ni-GaAs diffusion couples to be 1.47×10^{-11} cm²/s at 300°C, which would result in a characteristic diffusion length (\sqrt{Dt}) of 7500Å for a 6.5 min anneal. This characteristic diffusion length is much larger than the Ni₃GaAs layer thickness (~1000Å). This suggests that the rate of supply of Ni to the surface as a result of diffusion out of the Ni₃GaAs is not the limiting factor for the NiAs formation rate. Whether the NiAs growth occurs at

the surface by Ni outdiffusion or at the NiAs/Ni₃GaAs interface by As diffusion through the NiAs has yet to be determined.

Possible models for the reaction mechanisms in reactions (1) and (2) can be suggested. In reaction (1) the Ni₃GaAs forms as a result of Ni indiffusion with Ga and As remaining essentially immobile at 300°C. When the surface of Ni₃GaAs is exposed to As₄, the chemical potential for Ni is lower in NiAs than in Ni₃GaAs (the driving force for reaction (2)) and Ni diffuses out of the Ni₃GaAs to form NiAs on the surface. As the Ga and As atoms have essentially remained immobile during the process, GaAs regrows as the Ni leaves the Ni₃GaAs. One may think of the GaAs acting as a sponge for the Ni.

The model can also explain the precipitate formation in the regrown GaAs. By comparing the micrographs in Fig. 5(a) and (b), the spacing of the small vertical lines of inclusion in the regrown GaAs (Fig. 5(b)) can be seen to correspond to the grain boundary spacing of the Ni₃GaAs prior to the GaAs regrowth reaction (Fig. 5(a)). Hence, a reasonable argument can be made that these precipitates formed in the grain boundaries of the Ni₃GaAs prior to the regrowth reaction (2). Thermodynamics dictates that there is a driving force for Ni₃GaAs decomposition into NiGa and NiAs. Guivarc'h et al[13] observed that the initial decomposition involves the formation of two ternary Ni_xGa_{1-y}As_y phases, one richer in Ga and the other richer in As, which they label C and A, respectively. This decomposition can only occur through Ga or As diffusion, making precipitate formation easier at grain boundaries than in the bulk. The long annealing time (10 min) at 300°C prior to As₄ exposure would enhance Ni₃GaAs decomposition. If NiAs precipitates have formed, there is no driving force for the Ni to diffuse out of the precipitate to the surface in order react with the As₄ flux as it already is in the form of NiAs. As the activation energies for As and Ga interdiffusion in Ni_xGaAs are larger than for Ni[21], lower temperature would decrease the relative diffusion of Ga and As compared to Ni. Hence, shorter annealing times and lower annealing temperatures should result in a dramatic decrease in the precipitate density. Using the Ni interdiffusion coefficient reported by Chen et al.[8], a 20s anneal should be sufficient to complete reaction (1) at 300°C and 180s at 200°C.

3.3.3 Reaction (3): Ga reactions with Ni₃GaAs/GaAs

Thermodynamics suggests that Ga deposition on the Ni₃GaAs/GaAs structure should also induce a GaAs regrowth reaction. The streaked RHEED pattern of Ni₃GaAs began to show spots within 2 min exposure to $\sim 2.4 \times 10^{13}$ atoms cm⁻²s⁻¹ Ga flux with the sample at 350°C. The pattern began showing streaks again after 30 min. The RHEED patterns were consistent with the formation of an epitaxial Ni₂Ga₃ layer. The x-ray diffraction patterns show a decrease in (10̄1)Ni₃GaAs peak intensity and an increase in the (10̄1)Ni₂Ga₃ peak as reaction (3) progresses in a similar manner to the regrowth reaction induced by an As₄ flux (reaction (2)). The RBS results are consistent with a Ni₂Ga₃/Ni₃GaAs/GaAs/Ga_{0.5}Al_{0.5}As/GaAs layered structure.

In order to achieve high uniformity, the regrowth reaction should be limited by the As₄ or Ga arrival rate. This ensures no accumulation of unreacted species at the surface during the reaction. The sticking coefficient for As₄ depends upon the surface composition. At 300°C As₄ will not stick on the surface unless it reacts with Ga or Ni. This ensures that excess As₄ will not accumulate on the surface, making reaction (2) self-limiting. This is not the case for Ga, as the Ga sticking coefficient is approximately unity independent of surface composition.

RBS studies of reaction (2) indicated that NiAs thickness and regrown GaAs thickness increased linearly as a function of As₄ exposure time, with the sample at 300°C and an As₄ flux of 1.2×10^{15} atoms cm⁻²s⁻¹. This implies that reaction (2) was limited by

the As_4 arrival rate. For Ga, an arrival rate of $\sim 2.4 \times 10^{13} \text{ Ga cm}^{-2}\text{s}^{-1}$, and a substrate temperature of 350°C was required to eliminate Ga accumulation on the surface. Hence, the diffusivity for Ni or Ga through Ni_2Ga_3 is about two orders of magnitude slower than for Ni or As in NiAs. The high crystalline quality of the epitaxial Ni_2Ga_3 may result in a substantial reduction in fast diffusion paths such as grain boundaries.

3.3.4 In-situ Electrical Measurements

A key issue is to determine the electronic properties of the regrown GaAs and the metal/regrown-GaAs interface. We developed procedures for in-situ contact formation using a removable shadow mask and electrical measurements. Fig. 7 shows the MBE system setup used for the shadow mask deposition and in-situ electrical measurements.

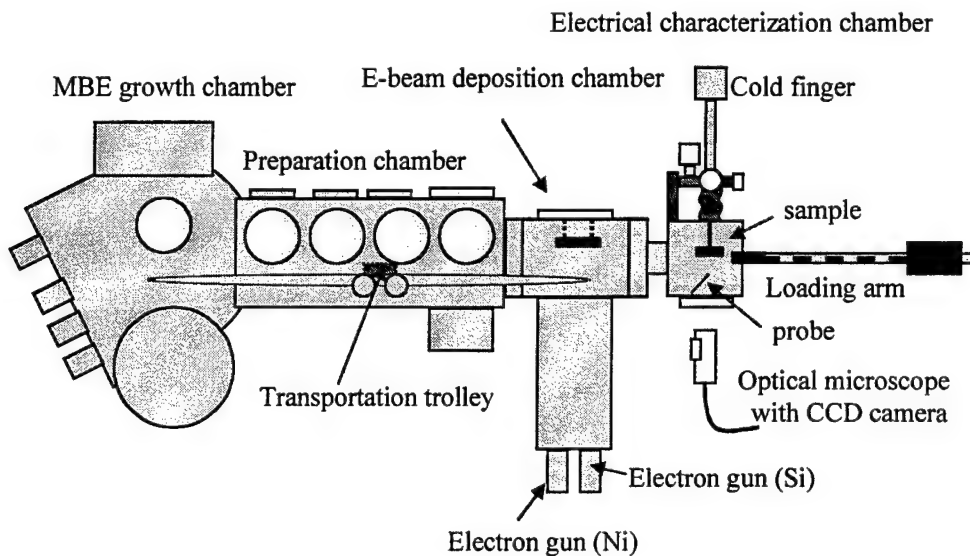


Fig. 7 Schematic drawing of the modified VG Semicon V80H MBE system for in-situ shadow mask deposition and electrical characterization.

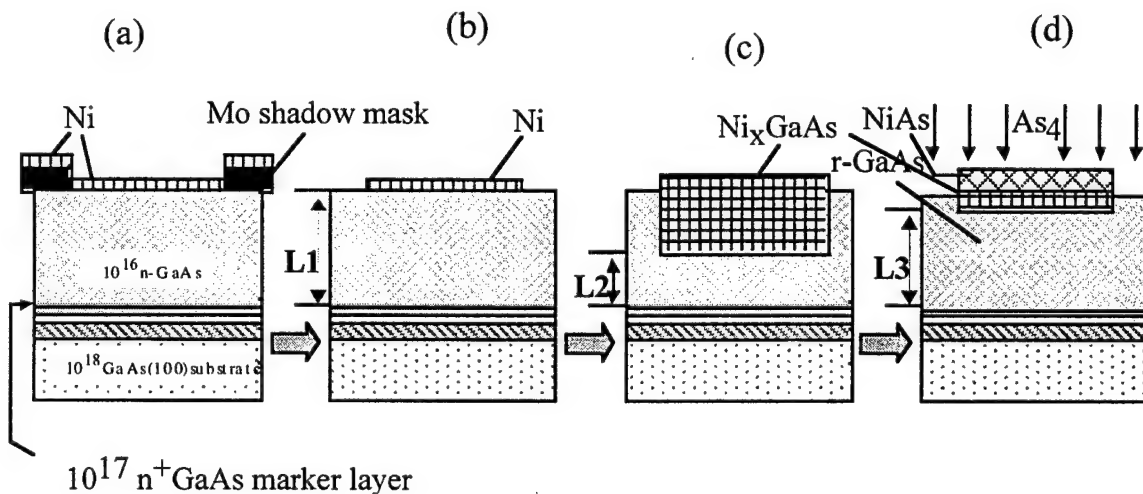


Fig. 8 Sequential reaction procedure: (a) depositing Ni through a Mo shadow mask; (b) after mask removal; (c) after reaction (1) induced by 300°C annealing; (d) after regrowth reaction (2) induced by As_4 exposure at 350°C .

The shadow mask deposition and subsequent reaction process is shown in Fig. 8. Fig. 9 shows a schematic of the probe station that was built to make in-situ I-V and C-V measurements and Fig. 10 an optical micrograph showing the probe and a shadow masked patterned sample.

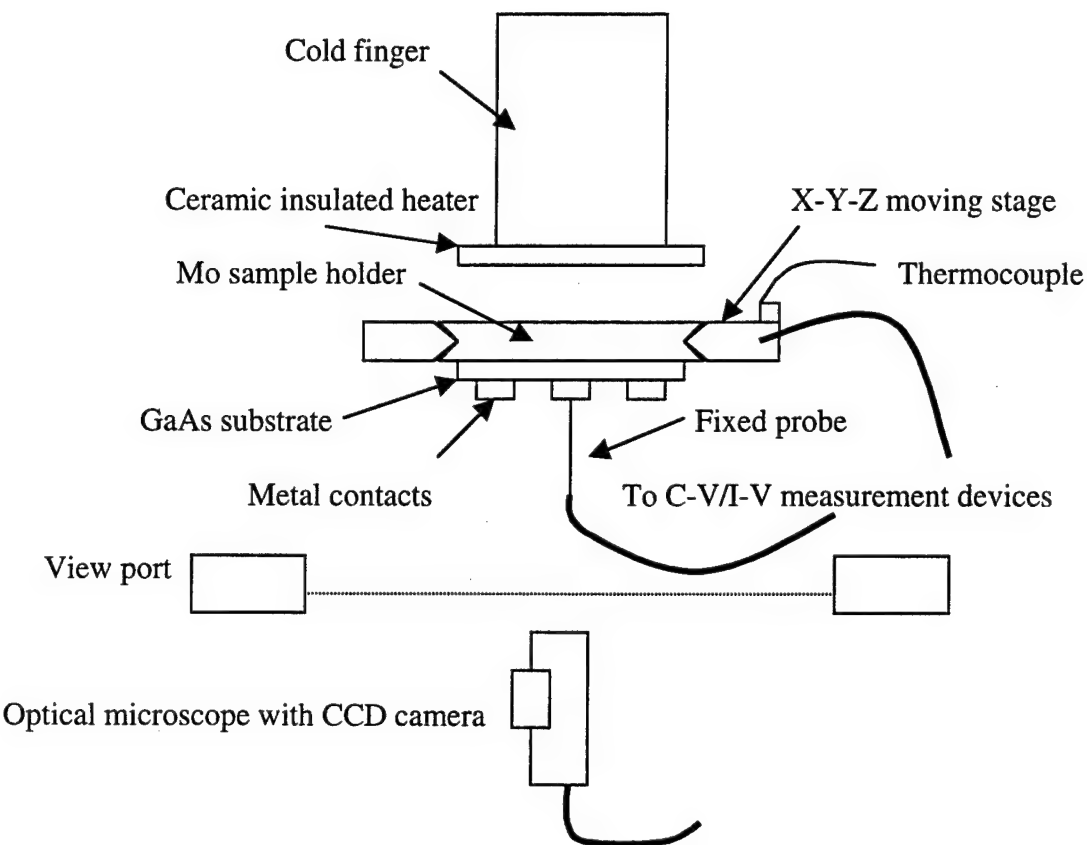


Fig. 9 Schematic drawing of the *in-situ* electrical characterization.

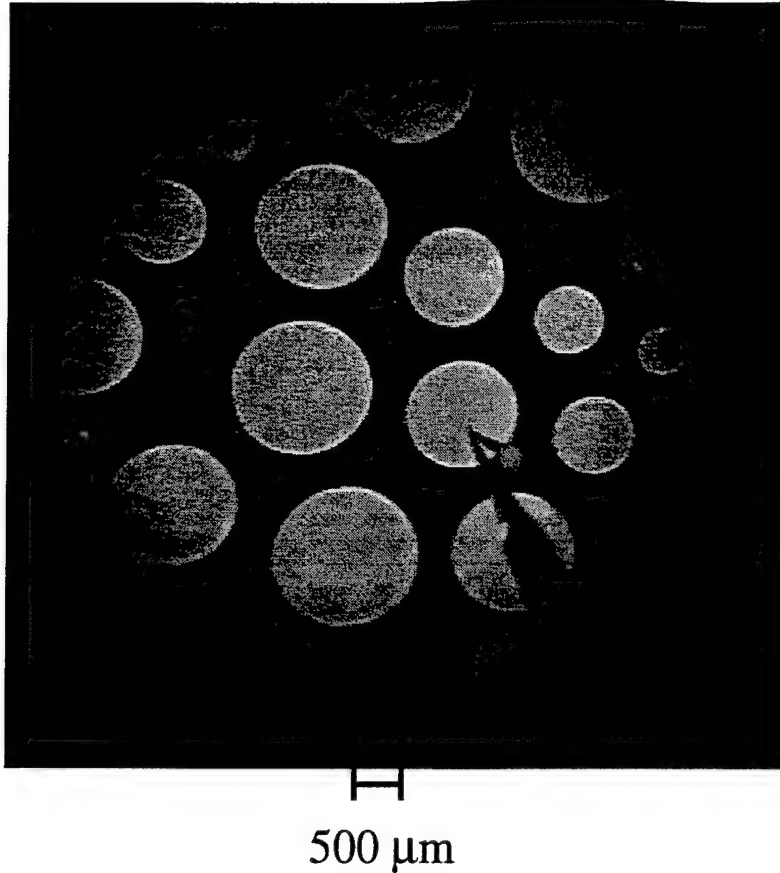


Fig. 10 The *in-situ* patterned Ni dot array with 10 different sizes ranging from $\sim 500\mu\text{m}$ to $\sim 1400\mu\text{m}$ and an electrochemically etched W wire probe.

3.3.5 Schottky barrier height and Ideality Factor Measurements

In-situ forward biased I-V measurements of the same contact after different reaction stages are shown in Fig. 11. Similar results were found for all contacts. The average of the Schottky barrier heights and ideality factors are depicted in Fig. 12. The C-V Schottky barrier heights ($\phi_{bn,C-V}$) were determined from plots of $1/C^2$ vs. V with image force lowering correction and the I-V Schottky barrier heights ($\phi_{bn,I-V}$) were determined from the saturation current density[23]. The high ideality factor of the as-deposited Ni/GaAs contacts may result from either non-uniform interfacial reaction during contact formation[24] or possibly defects in the near surface region of the GaAs induced during Ni deposition. For the NiAs/regrown-GaAs, the low ideality factor of $n \leq 1.11$ indicates that conduction is primarily dominated by thermionic emission[25] and that the electrical quality of the regrown-GaAs is high.

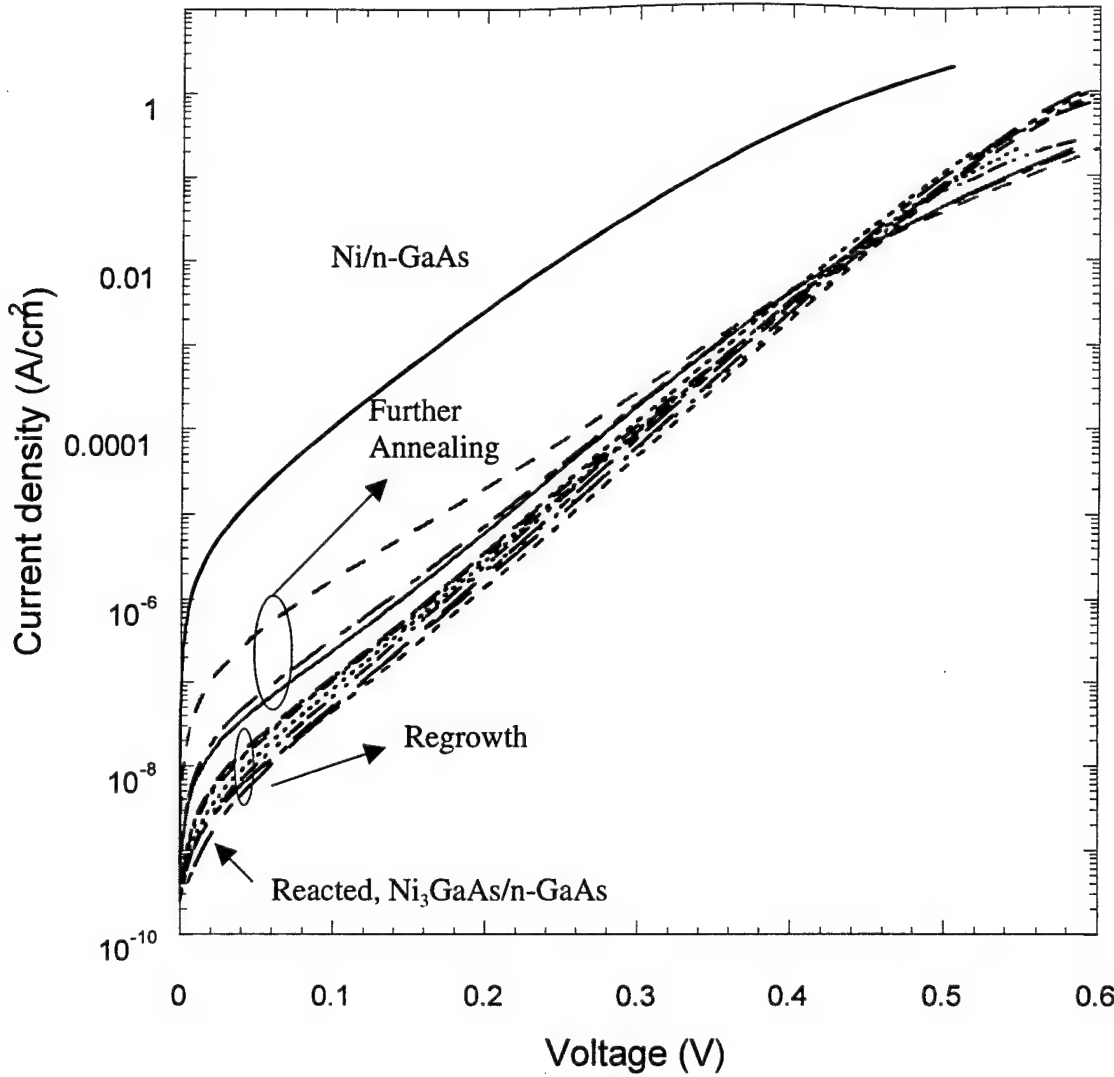


Fig. 11 *In-situ* current-voltage characterization of the same Ni/GaAs contact for as deposited, annealed at 300°C, exposure to As₄ at 350°C for different times.

The Schottky barrier height of Ni on MBE grown c(4x4) GaAs(100) was determined to be $\phi_{bn,I-V}=0.67\text{V}$ and $\phi_{bn,C-V}=0.73\text{V}$, from I-V and C-V measurements, respectively. When Ni was deposited on substrates which had not been cooled completely to room temperature (estimated substrate temperature ~100-150°C) a significantly higher barrier height was observed ($\phi_{bn,I-V}=0.77\text{V}$ and $\phi_{bn,C-V}=0.82\text{V}$). As the barrier height increases with Ni_xGaAs formation, the increased barrier height observed is consistent with the onset of interfacial reactions during the deposition. This may explain the discrepancy in barrier height between the as-deposited Ni/n-GaAs(100) ($\phi_{bn,I-V}=0.67\text{V}$ and $\phi_{bn,C-V}=0.73\text{V}$) reported here and the Ni deposited on the thermally-cleaned GaAs(100) ($\phi_{bn,I-V}=0.77\text{V}$ and $\phi_{bn,C-V}=0.91\text{V}$)[26,27].

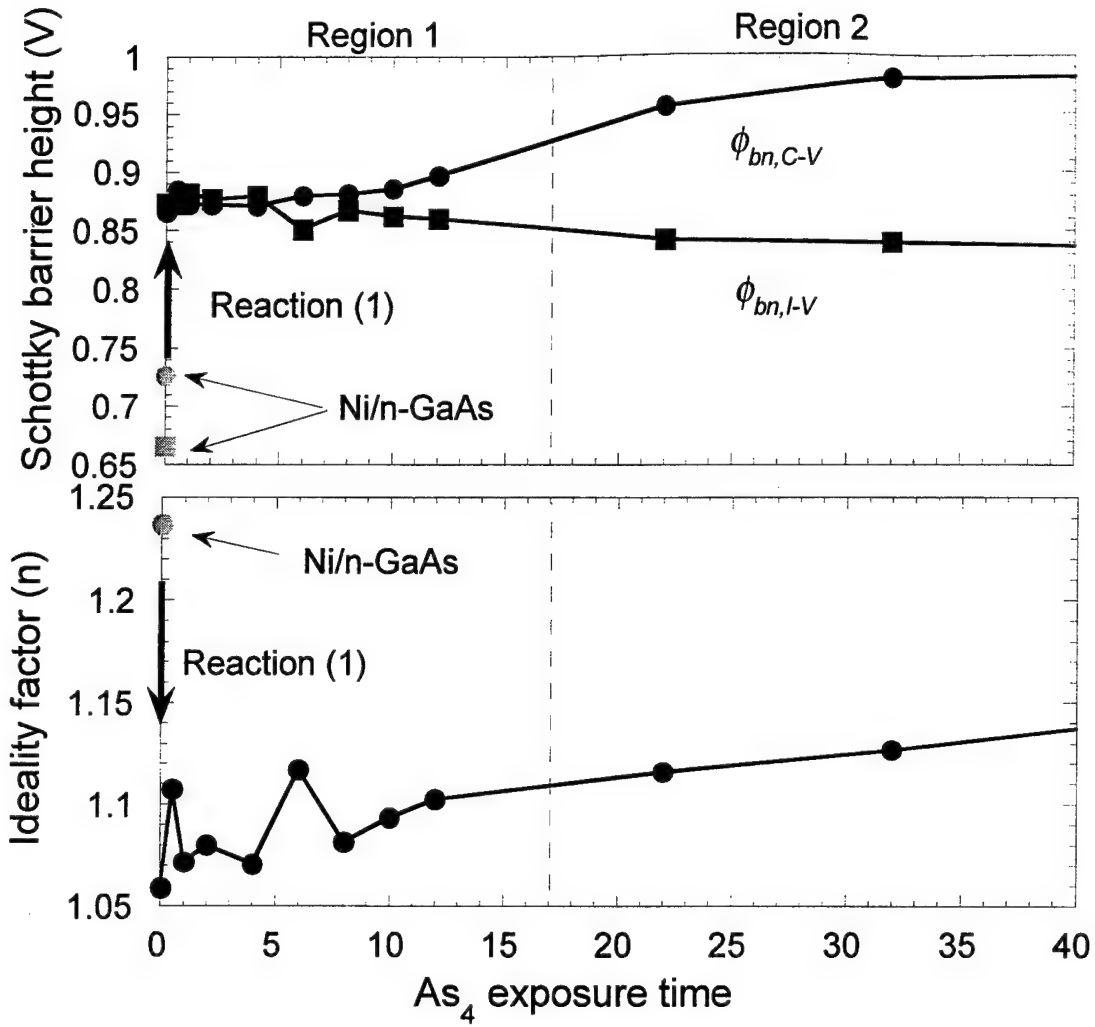


Fig. 12 Summary of averaged Schottky barrier height and ideality factor obtained from *in-situ* C-V and I-V measurements.

When the Ni/GaAs structure is annealed at 300°C, Ni_xGaAs forms and the Schottky barrier height increases ($\phi_{bn,I-V}=0.87\text{V}$ and $\phi_{bn,C-V}=0.87\text{V}$). This value is similar to that reported for *ex-situ* annealing ($\phi_{bn,I-V}=0.83\text{V}$ [28] and $\phi_{bn,C-V}=0.82\text{V}$ [29]). After the As_4 -induced regrowth reaction at 350°C, the barrier height from I-V measurements remains approximately constant for different As_4 exposure times ($\phi_{bn,I-V}\approx0.85\text{V}$), whereas the barrier height from C-V measurements increased. As shown in Fig. 12, the Schottky barrier height discrepancy between I-V and C-V measurements increased with As_4 exposure time. A possible explanation is an increase in the inhomogeneity of the Schottky barrier height in the contacts[24,30]. However, the low ideality factor, $n\leq1.11$,

suggests a relatively homogeneous contact. An alternative explanation could result from the properties and increased thickness of the regrown-GaAs, which is discussed below.

3.3.6 Doping depth profiles

Fig. 13 shows the doping depth profiles obtained from C-V measurements using the conventional assumptions for depletion width, w , (equation (4)) and doping concentration[25] for the same sample after Ni deposition, reaction, and different As_4 exposure times. With these assumptions, the depletion width is given by

$$w = \frac{\epsilon_s}{C} \quad (4)$$

where ϵ_s is the semiconductor dielectric constant and C the measured capacitance per unit area. The depth of the doping spike in the doping depth profile represents the distance between the marker layer and metal/GaAs interface.

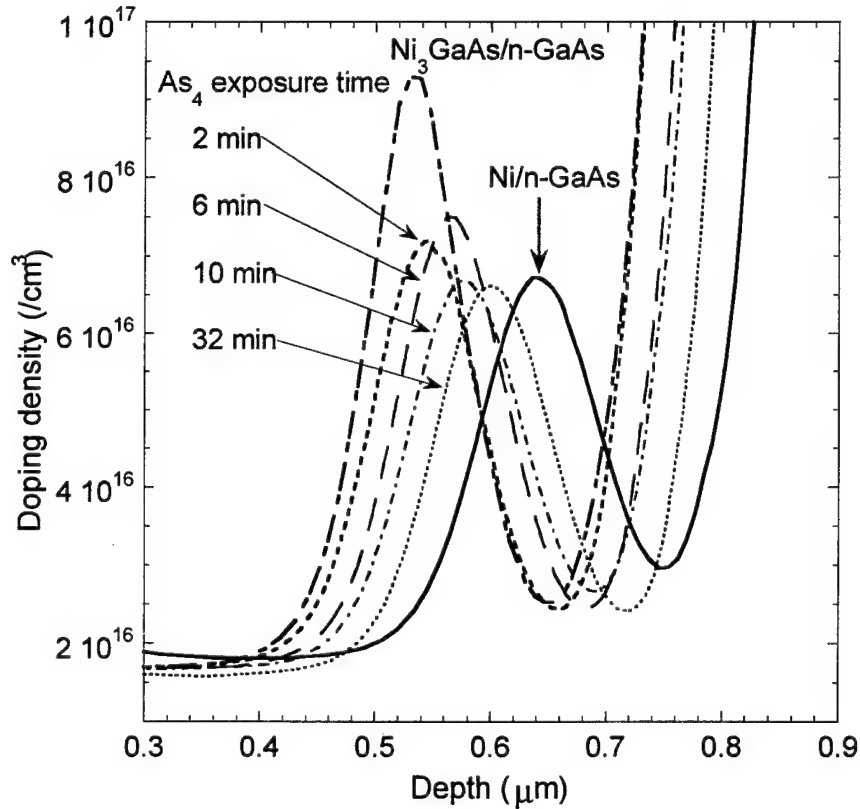


Fig. 13 In-situ C-V doping depth profiles from Ni/GaAs contacts of as-deposited, reacted at 300°C, and subsequent As_4 exposure at 350°C for different times. The depletion depth was obtained from equation (4).

The profile for the as-deposited Ni/GaAs structure shows the n^+ marker layer at depth of 0.641 μm beneath the metal/GaAs interface (L1 in Fig. 8(b)). Upon annealing at 300°C

without As_4 exposure, the marker layer shifts to $0.534\mu\text{m}$ (L2 in Fig. 8(c)). This corresponds to a 1070\AA of GaAs consumption (the difference between L1 and L2 in Fig. 8). When subsequent annealing is performed with the As_4 flux, the marker layer moves deeper and closer to its original position, indicating that the distance between the marker layer and metal/GaAs interface increases with As_4 exposure time. Fig. 14 shows the GaAs regrowth thickness obtained from the measurements of the n^+ marker layer position for different As_4 exposure times and from the RBS measurements on other samples (Fig. 6). The solid data points came from doping depth profiles which used equation (4) for determining the depletion width. There are two distinct regions in the GaAs regrowth. It appears that no GaAs regrowth occurs for annealing with an As_4 flux for time ≤ 60 sec. This apparent lack of regrowth may result from the regrown layer being thinner than depth resolution of the C-V depth profiling technique (Debye length $\sim 300\text{\AA}$) or from no actual regrowth. The latter possibility could occur if Ni outdiffused from the Ni_3GaAs to form NiAs on the surface, leaving behind a Ni_xGaAs ($x < 3$) phase without inducing GaAs regrowth. Evidence for a change in Ni concentration during growth comes from the observed change in Ni_xGaAs lattice parameters with As_4 exposure. Longer As_4 exposure times result in an increase in the regrown layer thickness. For exposure times ≥ 20 min (region 2), no more GaAs regrowth on the GaAs substrate occurs, indicating that the regrowth reaction has come to completion. This suggests that the GaAs regrowth reaction (reaction (2)) stops after 15-20 min of As_4 exposure time. The data obtained using equation (4) (● dots in Fig. 14) indicate that 410\AA GaAs does not regrow on GaAs substrate. This may result from the metallurgical interface not being the same as the electrical interface, GaAs clusters or Ga dissolution in the NiAs, or from the method used to obtain the doping depth profile from the C-V measurements. As Ni is believed to be the dominant diffusing species at this temperature, it is difficult to envisage a reaction mechanism that results in GaAs formation in the NiAs. The RBS data and Auger depth profiles from this sample show no Ga incorporation in the NiAs. As discussed above, RBS and TEM results on other samples suggest that complete regrowth takes place. It is interesting to note that if the GaAs regrowth thickness were extrapolated from the RBS results, the complete GaAs regrowth would occur after ~ 17 min of As_4 exposure (Fig. 14), which is comparable to that determined from the C-V depth profiles. Therefore, the 410\AA thickness discrepancy is believed to arise from the method used to obtain depth profiles from C-V measurements. Hence, the electrical properties of the regrown-GaAs and their effects on the electrical measurements must be determined. If the regrown-GaAs has a different dielectric constant from the unreacted-GaAs, equation (4) is no longer valid. As the regrown-GaAs and unreacted-GaAs will act as series capacitors, the capacitance per unit area will be given by[31]:

$$\frac{1}{C} = \frac{t}{\epsilon_{\text{regrown}}} + \frac{w-t}{\epsilon_s} \quad (5)$$

where t is the regrown-GaAs layer thickness, $\epsilon_{\text{regrown}}$ the dielectric constant of regrown-GaAs, and w the depletion width. The relationship between the measured depletion width ($w_m = \epsilon_{ss}/C$) and measured regrown layer thickness (t_m) obtained using equation (4) and the true depletion width (w) and regrown layer thickness (t) obtained from equation (5) is given by:

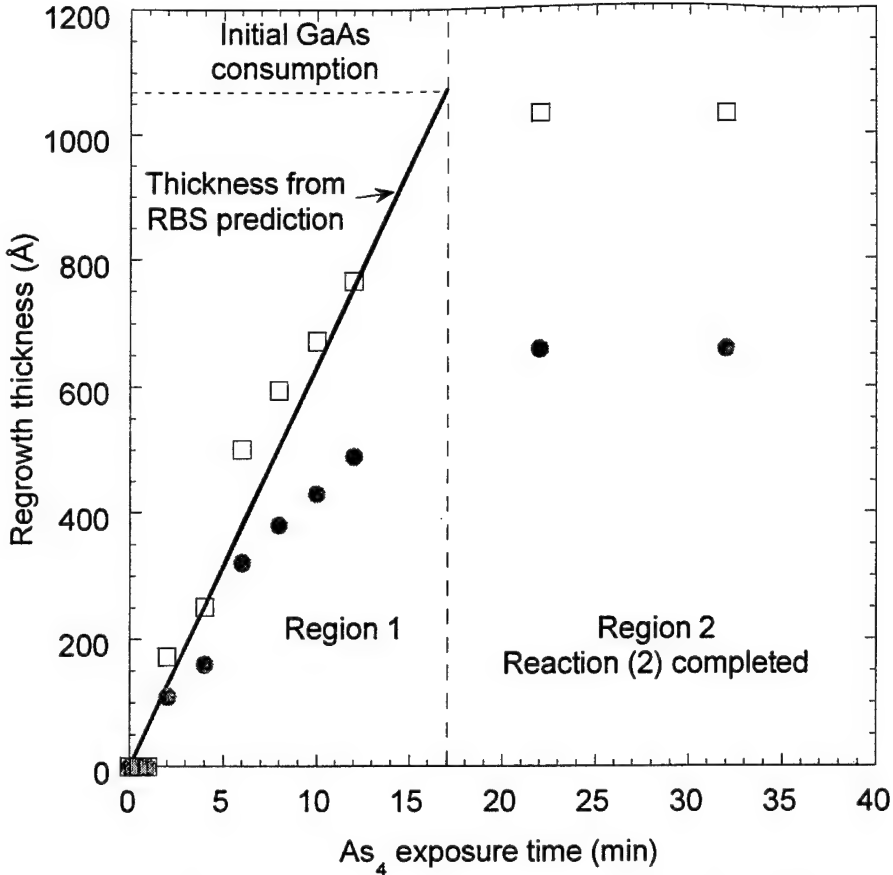


Fig. 14 GaAs regrowth thickness obtained from *in-situ* C-V doping depth profiles (data points) and *ex-situ* RBS results. The □ and ● data points represent the regrown-GaAs thickness calculated from equation (4) and equation (5), respectively.

$$w_m - w = t_m - t = \left(\frac{\epsilon_s}{\epsilon_{regrown}} - 1 \right) t \quad (6)$$

and

$$t = \frac{\epsilon_{regrown}}{\epsilon_s} t_m \quad (7)$$

By assuming that all the GaAs regrows on the GaAs substrate, the regrowth depends on the As₄ arrival and the regrowth reaction completes in ~17 min, the true regrown-GaAs thickness can be predicted. The dielectric constant of the regrown-GaAs can then be determined from the slope of t versus t_m plot (Fig. 15). A slope of 1.56 suggests a 56% increase in the dielectric constant of the regrown-GaAs as compared to GaAs, *i.e.*, $\epsilon_{regrown} = 20.5 \epsilon_0$, which would result in the underestimation of the regrown-GaAs thickness using equation (3). The recalculated doping depth profiles (Fig. 16) show that the n⁺ marker layer has shifted back to its original position after 32 min of As₄ exposure, indicating that the GaAs is fully regrown on the substrate. The open square (□) data points in the Fig. 14 shows the dielectric constant modified regrown-GaAs thickness with As₄ exposure.

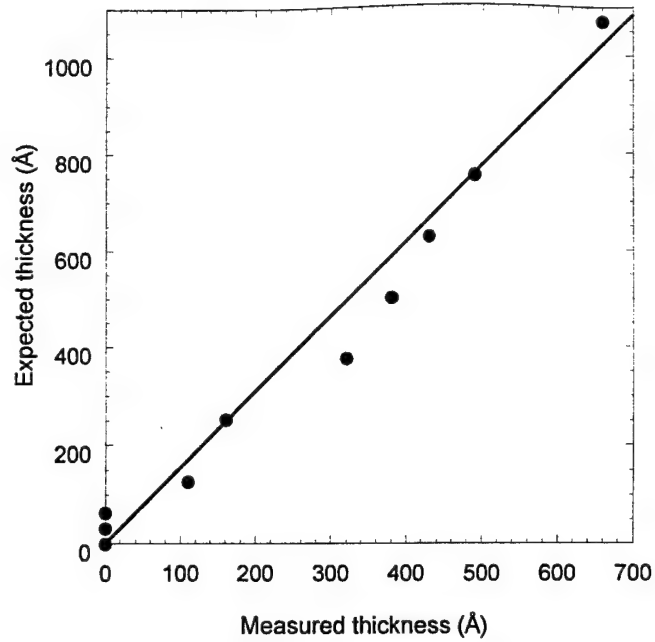


Fig. 15 The linear dependence of t on t_m shows the interlayer dielectric constant of $\epsilon_{regrown} \sim 20.5\epsilon_0$.

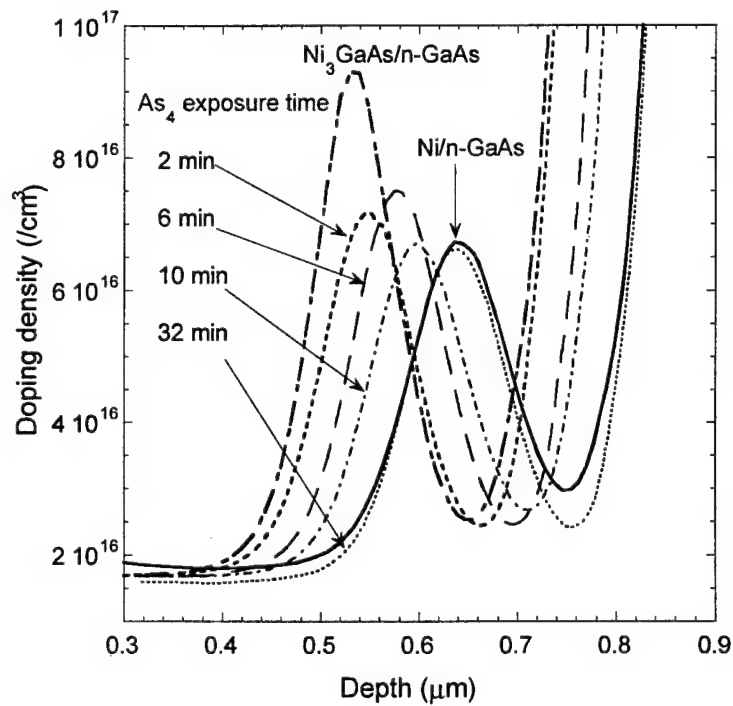


Fig. 16 Doping depth profiles obtained from C-V measurements. The depletion depth for samples with regrown-GaAs was calculated using equation (5), the dielectric constant modified depletion width.

incorporation, which is a deep acceptor in GaAs, and point and structural defects in the regrown-GaAs. These would be expected to increase the leakage current and ideality factor due to trap-assisted tunneling through the barrier. The low ideality factor, $n \sim 1.11$, for the regrown contacts suggests that this is not the case. This is particularly surprising as the TEM results indicated stacking faults and precipitates in the regrown-GaAs (Fig. 5), which are assumed to be NiAs. Although the precipitates do not appear to influence the transport properties significantly, such precipitates may be the cause of the proposed high dielectric constant of the regrown-GaAs. Unfortunately, the low doping concentration and thin layer thickness of the regrown-GaAs made direct doping density determination from C-V measurements impossible as it was always completely depleted.

Fig. 17 shows schematic sketches of a metal/regrown-GaAs(interlayer)/n-GaAs structure and its band diagram. The doping and the dielectric constant of the regrown

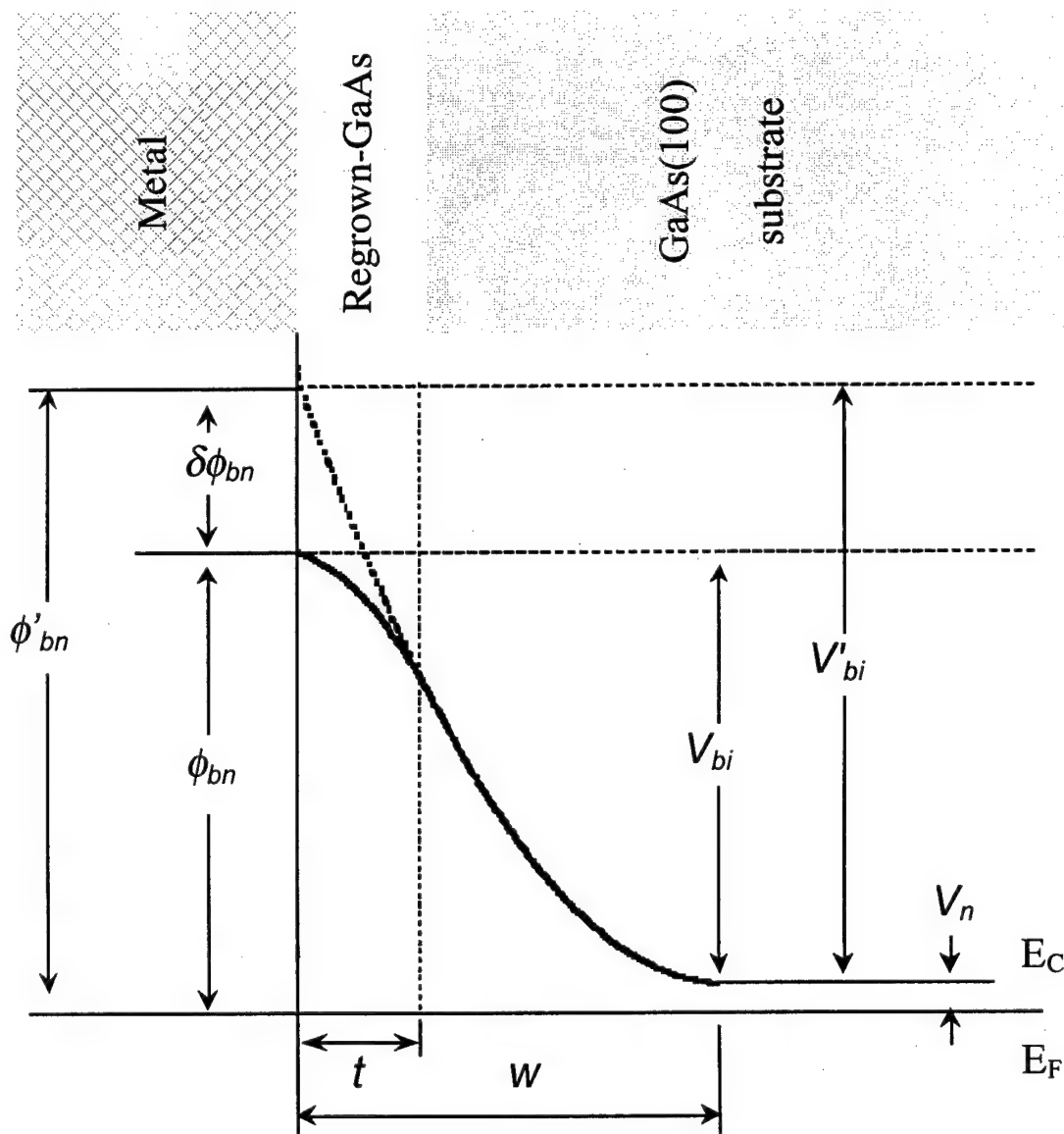


Fig. 17 Simulation of band bending with (solid line) and without (dashed line) interlayer. ($N_D = 2 \times 10^{16}/\text{cm}^3$, $N_i = -3 \times 10^{16}/\text{cm}^3$ (p-type), and $t = 1000\text{\AA}$)

GaAs are different from the n-GaAs. In order to verify this model, the expected barrier height with interlayer thickness t must be determined by solving Poisson's equation with the appropriate boundary conditions. In addition to the usual boundary conditions[25], the doping density and dielectric constants are assumed to be constant, N , $\epsilon_{regrown}$ in the interlayer and N_D , ϵ_s in the remaining semiconductor. Solving Poisson's equation gives the electric field at the metal/semiconductor interface, E_m .

$$-E_m = \frac{qN_D}{\epsilon_s}(w - t) + \frac{qN_t}{\epsilon_{regrown}}t \quad (8)$$

the built-in potential, V_{bi} ,

$$V_{bi} = \frac{qN_D}{2\epsilon_s}w^2 + \left(\frac{qN_t}{2\epsilon_{regrown}} - \frac{qN_D}{2\epsilon_s} \right)t^2 \quad (9)$$

for $0 \leq x \leq t$, $V(x)$

$$V(x) = -E_m x - \frac{qN_t}{2\epsilon_{regrown}}x^2 \quad (10)$$

and for $t \leq x \leq w$, $V(x)$

$$V(x) = \left(-E_m + \frac{qN_D}{\epsilon_s}t - \frac{qN_t}{\epsilon_{regrown}}t \right)x - \frac{qN_D}{2\epsilon_s}x^2 + \frac{qN_t}{2\epsilon_{regrown}}t^2 - \frac{qN_D}{2\epsilon_s}t^2 \quad (11)$$

where $V(x)$, q , t , and w are electric potential, electron charge, interlayer thickness, and depletion width, respectively.

If there is no interlayer, i.e. $t = 0$, the equations reduce to the usual equations for a uniform Schottky barrier without an interlayer. However, if the interlayer is heavily p-doped, it can be shown that the energy band profile would reach a maximum at $x = \xi$, where

$$\xi = \frac{-E_m \epsilon_{regrown}}{qN_t} = \frac{N_D \epsilon_{regrown}}{N_t \epsilon_s} (w - t) + t \quad (12)$$

and $0 \leq \xi < t$. This results in a Schottky barrier height given by

$$\phi_{bn} = V_{bi} + V_n + \frac{kT}{q} + E_m \xi + \frac{qN_t}{2\epsilon_{regrown}} \xi^2 \quad (13)$$

and the extrapolated Schottky barrier height obtained from extrapolating the band bending at w is given by

$$\phi'_{bn} = V'_{bi} + V_n + \frac{kT}{q} \quad (14)$$

where

$$V'_{bi} = \frac{qN_D}{2\epsilon_s}w^2 \quad (15)$$

This extrapolated barrier height is identical to that for an uniform Schottky contact to N_D doped GaAs with a depletion width, w , neglecting image force lowering. Therefore, the Schottky barrier height discrepancy between I-V and C-V measurements can be described as $\delta\phi_{bn} = \phi_{bn} - \phi'_{bn}$ where ϕ'_{bn} and ϕ_{bn} do not include an image force lowering term. Fig. 17 shows the simulated band bending from the equations above. It is clear that the thicker the interlayer, the larger Schottky barrier height discrepancy between C-V and I-V measurements. Since Ni is a deep level acceptor in GaAs[32], it is reasonable to assume that the interlayer will not be heavily p-doped, so that the potential maximum will be close to the metal/semiconductor interface (i.e. $\xi \sim 0$) and the Schottky barrier height discrepancy can be simplified to:

$$\delta\phi_{bn} = \frac{qN_D}{2\epsilon_s} \left(1 - \frac{N_t\epsilon_s}{N_D\epsilon_{regrown}} \right) t^2 \quad (16)$$

This equation predicts that the Schottky barrier height discrepancy would be linearly dependent on the square of the regrown-GaAs thickness. As inhomogeneous barrier heights will also result in barrier height discrepancy between I-V and C-V measurements, the intrinsic Schottky barrier heights (ϕ_{bn}), which take into account inhomogeneous barrier heights and image force lowering, were determined from the I-V measurements using the procedure in reference [33] and [34]. Fig. 18 shows a plot of $\delta\phi_{bn}$ versus t^2 . Since there is no inhomogeneous correction for the C-V measurements, the data in Fig. 18 were fitted to

$$\delta\phi_{bn} = \frac{qN_D}{2\epsilon_s} \left(1 - \frac{N_t\epsilon_s}{N_D\epsilon_{regrown}} \right) t^2 + \delta\phi'_{bn} \quad (17)$$

where $\delta\phi_{bn}$ is to account for any barrier height inhomogeneity in the C-V measurement. The fit (solid line) gives the regrown-GaAs as p-type with doping density of $\sim 3 \times 10^{15}/\text{cm}^3$, which is consistent with Ni being a deep acceptor in GaAs, and $\delta\phi_{bn} \sim 0.005\text{V}$. Hence, the barrier height discrepancy between I-V and C-V measurements can be explained by the regrown-GaAs being p-type. This procedure enabled the electrical properties of the regrown-GaAs to be inferred without direct measurement.

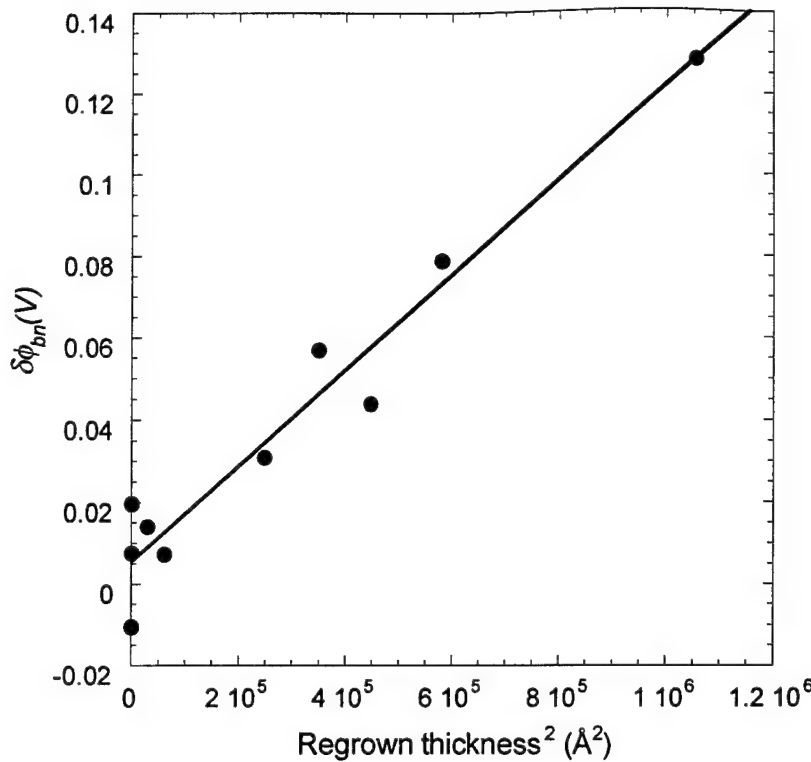


Fig. 18 Dependence of Schottky barrier height discrepancy ($\delta\phi_{bn}$) on the square of the interlayer thickness (t^2). The dots are data points obtained from *in-situ* electrical measurements and the line is linear curve fit to equation (17), indicating a p-type interlayer with $\sim 3 \times 10^{15}/\text{cm}^3$ doping and $\delta\phi_{bn}=0.005\text{V}$.

4 Nucleation and Growth and Properties of Epitaxial $\text{Fe}_x\text{Al}_{1-x}$ films

4.1 Introduction

The stable epitaxial growth of metals on III-V's is important to metal/semiconductor devices that need to operate at high temperature and to buried metal layer devices where interdiffusion at interfaces cannot be permitted. However, most metals that can be grown epitaxially on III-V's are not thermodynamically stable so that even modest heating causes reaction and interdiffusion at the interface. As discussed in section 3, metallic compounds containing group-III or group-V elements may be thermodynamically stable. We [35,36] have reviewed these issues and discussed other criteria necessary for stable epitaxial growth of metals on III-Vs. The main conclusion is that binary intermetallics that are lattice matched to III-V's and which can coexist with the III-V according to bulk phase diagram are candidate materials. Experiment has confirmed many of these ideas (section 3) [35,36], but the interplay of kinetics and thermodynamics as well as the details of the growth mechanisms has not been worked out. The main purpose of this report is to combine scanning tunneling microscopy (STM) with reflection high energy electron diffraction (RHEED) to study these competing issues.

Two major groups of intermetallics have been found to form stable epitaxial films. The first group has a cubic CsCl (B2) crystal structure and are known collectively as transition metal - three (TM-III) intermetallics. Some notable examples include NiAl, CoAl, FeAl, NiGa and CoGa. Their lattice parameters are usually 1-3% larger than one

half the lattice parameter of GaAs and their CsCl phases usually exists over a wide composition range. For $\text{Fe}_x\text{Al}_{1-x}$, the lattice mismatch is 2.9% and the range over which the phase exists is $0.5 < x < 0.63$. The second major group has a NaCl (B1) structure and are known collectively as rare earth - five (RE-V) intermetallics. Some notable examples include ErAs, LuAs and (Sc,Er)As. Their lattice mismatch is generally smaller, less than 2%. In this paper we examine the $\text{Fe}_x\text{Al}_{1-x}$ system because, in addition to the CsCl phase, it has a stable BiF_3 (DO_3) phase that is also reasonably well lattice matched to GaAs. This BiF_3 phase exists over the composition range, $0.63 < x < 0.78$ [37] and has a lattice mismatch of 2.4% [38]. It has been shown to form stable epitaxial films on AlAs up to 550°C [39,40], and has even been successfully grown directly on GaAs [41,42]. $\text{Fe}_x\text{Al}_{1-x}$ is particularly interesting since it becomes ferromagnetic at compositions above $x=0.7$. This makes it possible for $\text{Fe}_x\text{Al}_{1-x}$ to be used for magnetic metal/semiconductor devices. Further, its magnetic properties can be varied in a given structure simply by varying its composition.

In this report we investigate nucleation, annealing, growth and magnetic properties of $\text{Fe}_x\text{Al}_{1-x}$ films spanning both the CsCl and BiF_3 composition range, $0.5 < x < 0.78$. Previous work by Kuznia and Wowchak used RHEED and Auger electron spectroscopy to study the nucleation and growth of $\text{Fe}_x\text{Al}_{1-x}$ on pseudomorphic AlAs on InP(100) [39] and on AlAs/GaAs(100) [40]. They reported several main results. First, the initial nucleation exhibits an incubation period lasting 2 to 3 bilayers in which the intensity of the diffraction pattern decreases to near zero and then recovers. Second, growth of $\text{Fe}_x\text{Al}_{1-x}$ on an annealed $\text{Fe}_x\text{Al}_{1-x}$ surface results in RHEED oscillations corresponding to the growth of a monolayer or a bilayer of $\text{Fe}_x\text{Al}_{1-x}$. As seen in Fig.19, a monolayer is

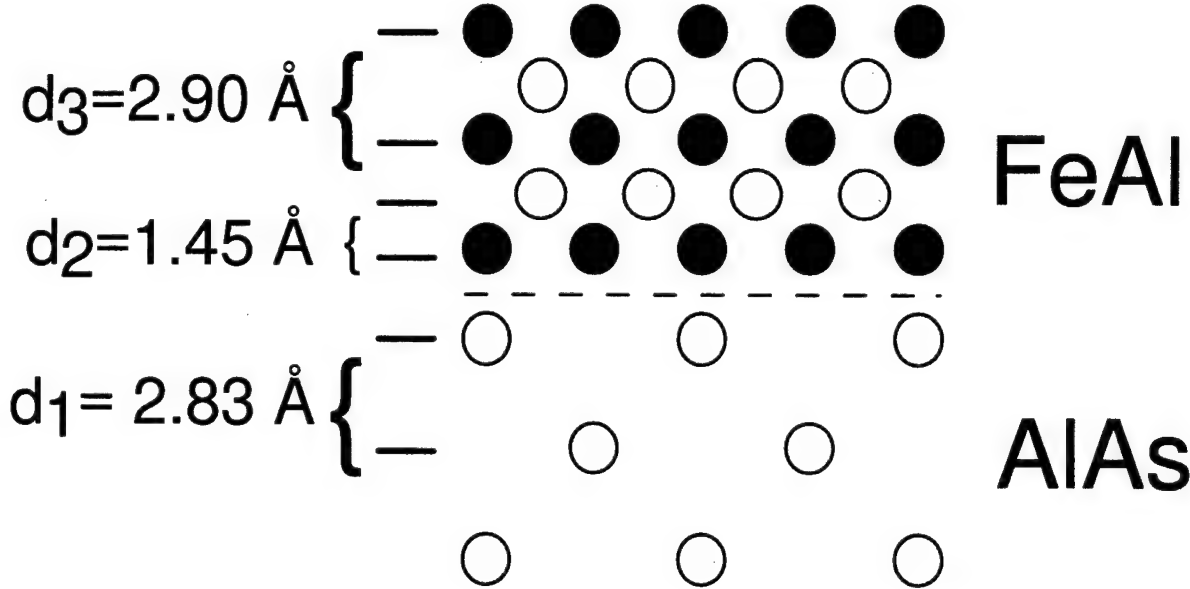


Fig. 19 Diagram showing an AlAs monolayer, d_1 , an FeAl monolayer, d_2 and an FeAl bilayer, d_3 .

defined as a one atom thick layer and a bilayer is defined as a two atom thick layer. In that work, however, it was difficult to extract quantitative information on surface morphology from the RHEED measurements, especially in the nucleation stage where the diffraction was weak and diffuse. In this work, we have applied ultrahigh vacuum STM

to obtain a real space view of the surface. We are able to use STM to examine a surface in which the RHEED pattern was diffuse. We use STM to extract step height and mean terrace lengths. In addition, we studied annealing and growth in more detail. Finally, we studied the magnetic properties of the films.

4.2 Experimental

A PHI-400 solid source MBE system was used for growth. Standard Knudsen cells were used for all sources except Fe, for which an electron bombardment source similar to that described by Jonker et al. [43] was used. The system was also equipped with a quartz crystal deposition monitor which could be positioned directly in front of the substrate. This was used to measure the Fe and Al flux prior to growth. In-situ growth monitoring was performed with a 10 keV RHEED system. The STM was housed in a separate chamber attached to the growth chamber. Samples could be transferred to this chamber without exposure to pressures above 10^{-8} Torr. MOKE measurements were performed in air using a laser with a wavelength of 650nm.

Epi-ready GaAs(100) n⁺ Si doped samples were cleaned by desorbing the oxide at 620°C in an As₄ background of 10^{-6} Torr. A 300 nm GaAs buffer, doped with Si to about 10^{18} cm^{-3} , was then grown. The buffer and substrate were doped to ensure that the sample would be conducting for STM measurements. After the GaAs buffer, 10 ML of AlAs was deposited at 540°C. With AlAs as an effective substrate, the thermodynamic stability argument regarding a three element system is expected to apply. The sample was cooled to 200°C and removed from the deposition chamber. The As source was cooled and the remaining As background was gettered with Ga and Al until the base pressure was below 3×10^{-9} Torr. The Fe and Al sources were then set to give the desired Fe-Al ratio using the quartz crystal deposition rate monitor. The sample was then returned to the deposition chamber and heated to 700°C until an AlAs (3x2) pattern appeared. This procedure was shown to drive off Ga surface contaminants and to reduce the As coverage on the surface [44]. Finally, the sample temperature was brought back down to 200°C and Fe_xAl_{1-x} was grown by co-deposition of Fe and Al.

To produce an epitaxial film, we deposited a minimum of 9 nm of Fe_xAl_{1-x} on the AlAs surface before annealing to between 550 and 700°C for 5 minutes. After annealing, additional Fe_xAl_{1-x} was grown at 200°C by again co-depositing Fe and Al. After growth of about 10 nm, the film was again annealed to between 550 and 700°C for 5 minutes. This process of growth and annealing could be repeated indefinitely without degradation of the RHEED pattern. During the growth of Fe_xAl_{1-x} on Fe_xAl_{1-x}, RHEED oscillations were obtained. From this we could obtain a composition ratio. This ratio was used as a verification of the ratio obtained from the quartz crystal deposition monitor and to insure that the Fe flux did not drift significantly. The value obtained from RHEED oscillations and the quartz crystal deposition monitor were within 5% of each other.

4.3 Results and Discussion

4.3.1 Nucleation

The intensity of the specular diffracted beam is shown versus time during the initial growth of FeAl on an AlAs buffer, Fig. 20. Here, Fe_xAl_{1-x} is co-deposited at a rate of 0.25 monolayers (ML) per second which corresponds to a period of 4.06 seconds per monolayer. The nucleation of the film is characterized by a near complete drop in the diffracted intensity followed shortly thereafter by a recovery and, in some cases, weak intensity oscillations. The starting RHEED pattern at t₁ is an AlAs (3x2). At t₂, after about 1 - 2 ML of deposition, the pattern is gone and the RHEED exhibits only a diffuse

background. With continued deposition a weak (1x1) $\text{Fe}_x\text{Al}_{1-x}$ pattern begins to develop. At t_3 , after 6 ML of deposition, the (1x1) pattern is now between 30 and 50% of the original intensity and remains near this intensity with continued deposition. The time period over which the diffraction pattern remains near zero is termed the incubation period and the time between when the pattern begins to recover and is fully recovered is termed the recovery period.

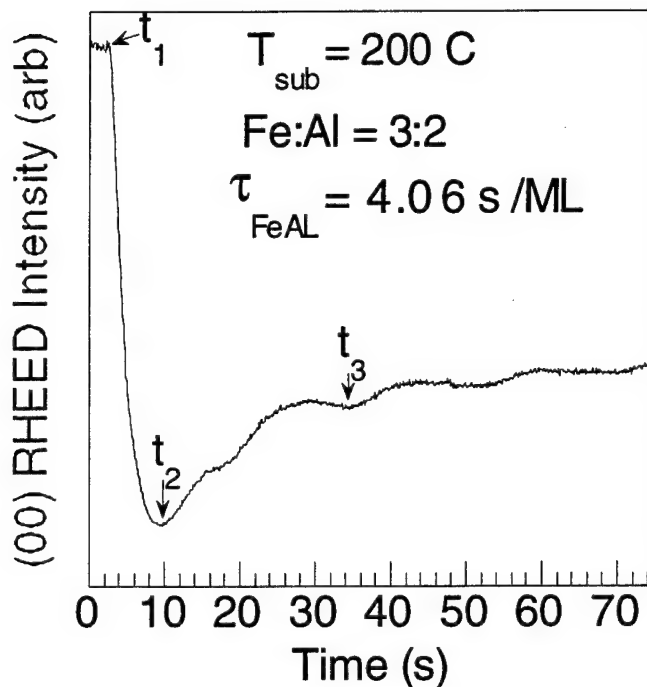


Fig. 20 RHEED intensity of the specular diffraction beam during initial nucleation of $\text{Fe}_x\text{Al}_{1-x}$ on AlAs. The starting pattern at t_1 is an AlAs (3x2) pattern. Growth is started at t_1 . At time t_2 , the RHEED pattern is no longer visible. At time t_3 , the intensity recovers to 30% of the original intensity and exhibits a broad and diffused (1x1) pattern.

Fig. 21a and b shows STM images taken after roughly 2 ML of growth. This corresponds to the point in the nucleation where the RHEED pattern intensity is a minimum. The first image, Fig. 21a, shows a long range scan. Large terraces, some greater than 120 nm in size, can be seen in this image. A close range scan, Fig. 21b, shows that the entire surface is covered with small features, 4 nm in size and approximately 0.2 nm high. These small features do not appear to be clearly resolved. Based on prior experience, this is likely due to a dull STM tip. Because of this, the real height values may be somewhat larger than the measured values. We interpret the large terraces observed in Fig. 21a to be due to the underlying AlAs surface and the small features due to $\text{Fe}_x\text{Al}_{1-x}$ clusters. We base this interpretation on the fact that similar shaped and sized terraces have been observed on a clean AlAs (3x2) surface with STM. Noting that there is only diffuse scattering in the RHEED pattern, we conclude that the small clusters are either disordered or randomly oriented on the AlAs surface.

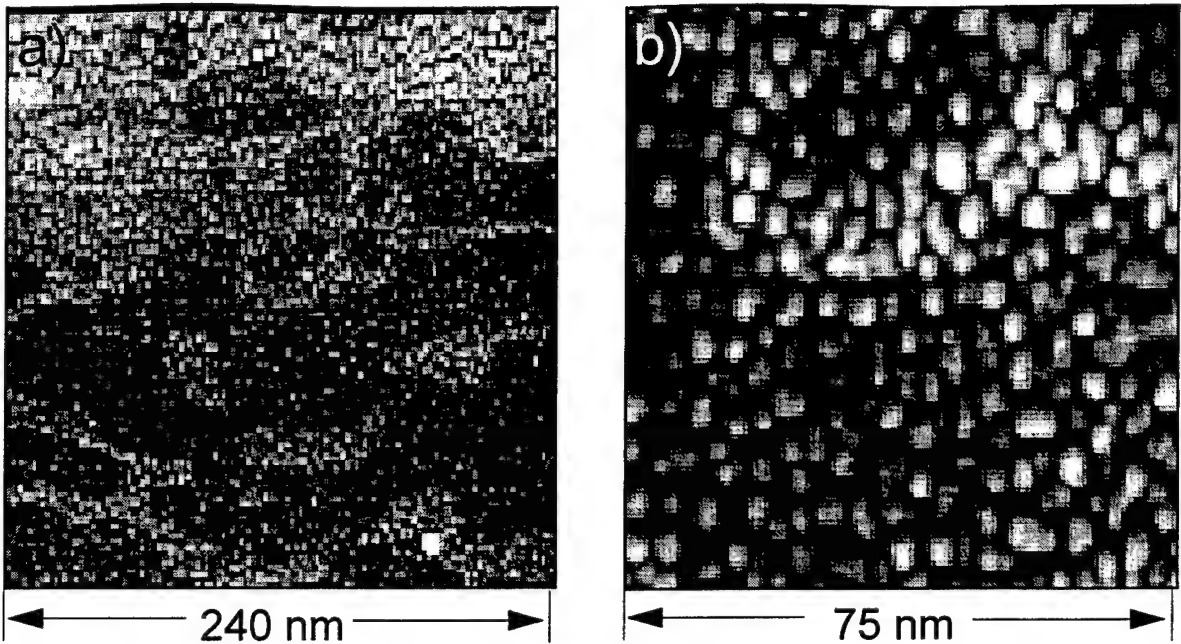


Fig. 21 STM images taken after 2 ML of growth. Terraces from the underlying AlAs surface can be seen in a) and small clusters of $\text{Fe}_x\text{Al}_{1-x}$ can be seen in b).

4.3.2 Annealing

At least 9 nm of $\text{Fe}_x\text{Al}_{1-x}$ was deposited on the AlAs surface at 200°C before annealing. Attempting to anneal films less than 9 nm thick commonly resulted in the inability to obtain RHEED oscillations during $\text{Fe}_x\text{Al}_{1-x}$ overgrowth. We found some evidence that the minimum thickness which can be annealed and still obtain RHEED oscillations during overgrowth was dependent on film composition. At lower Fe compositions, closer to $x=0.5$, we were able to anneal films as thin as 2 nm with satisfactory overgrowth results.

With $\text{Fe}_x\text{Al}_{1-x}$ growth on an annealed $\text{Fe}_x\text{Al}_{1-x}$ surface, RHEED oscillations died out after approximately 10 nm of growth at temperatures between 150 and 200°C. At this point, the film exhibited a broad and diffuse 1x1 diffraction pattern. An anneal was necessary to smooth the surface and make it possible to obtain RHEED oscillations with continued $\text{Fe}_x\text{Al}_{1-x}$ growth. We annealed to between 550 and 700°C and depending upon film composition and anneal temperature, the film exhibited either a sharp (2x2) and/or a sharp (5x5) diffraction pattern. A sharp (2x2) pattern would appear after annealing to 550°C for 5 min. The appearance of this pattern was not dependent on composition. However, annealing films to 650-700°C resulted in the composition dependent formation of a (2x2) and/or a (5x5) diffraction pattern. At $x = 0.5$, the film would exhibit a pure (2x2) pattern. Between $0.55 < x < 0.7$ the film would exhibit a combined (2x2) and (5x5) pattern with the 5-fold pattern becoming more and more dominant at higher Fe concentrations. This combined RHEED pattern was likely a superposition of diffraction patterns from regions of 5-fold ordering and other regions of 2-fold ordering. At or above $x = 0.75$, the film exhibited a pure (5 x) pattern.

We looked at the surface of two annealed films with UHV STM, one exhibiting a (2x2) diffraction pattern and one exhibiting a (5x5) pattern Fig. 22a and 22b show the images corresponding to the (2x2) surface. This film had the composition $\text{Fe}_{0.72}\text{Al}_{0.28}$

was annealed to approximately 550°C. Islands and terraces are clearly visible. The average island size is about 15 nm and average step heights is about 0.3 nm which roughly corresponds to one half the Fe₃Al lattice constant, 0.289 nm. Fig. 22c and 22d show STM images corresponding to a (5x) surface. This film had the composition Fe_{0.76}Al_{0.24} and was annealed to approximately 650-700°C. Here, few islands are visible, but terraces can be seen. The average terrace length is about 40 nm and the measured step height is approximately 0.3 nm. Comparing the two images, it is clear that the (5x5) has a much smaller step density than the (2x2) surface as is expected by a higher temperature anneal. However, the (5x5) surface also exhibits faceting along the [011] and the [011] directions causing the appearance of sharp 90° kinks in the step edges of the terraces.

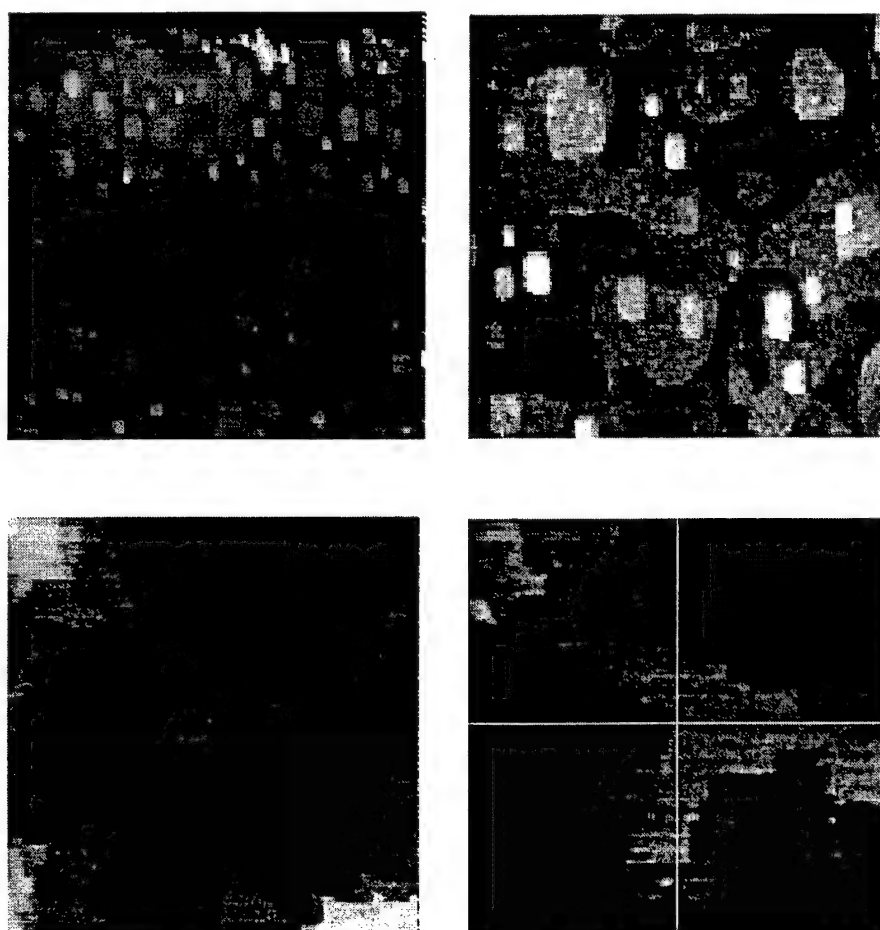


Fig. 22 Two STM images of an Fe_{0.72}Al_{0.28} surface annealed to approximately 550-C, a) and b), and two of an Fe_{0.74}Al_{0.24} surface annealed to approximately 650-700-C, c) and d). The sample from a) and b) exhibited a (2x2) diffraction pattern while from c) and d) exhibited a (5x5) diffraction pattern. Both surface exhibited bilayer high steps, but the step density in c) and d) is much smaller than in a) and b). Notice also the faceting in c) and d).

4.3.3 Growth

After annealing, $\text{Fe}_x\text{Al}_{1-x}$ was deposited at various compositions. Depending on the growth composition and the preparation of the surface, two different growth modes were observed, monolayer- and bilayer-growth, as determined by the period of the oscillations in the specular RHEED intensity. Compositions between $0.7 < x < 0.8$ always resulted in monolayer growth while compositions between $0.5 < x < 0.7$ resulted in either bilayer or a combined monolayer and bilayer growth. In this composition range, the annealed surface upon which we were growing had a large effect on growth mode. On a (2×2) surface, growth would be bilayer, however when attempting to grow on a surface exhibiting a (5×5) diffraction pattern, at least the first few layers would grow monolayer-by-monolayer. The duration of the monolayer growth was dependent on the growth composition. For example, at a composition of $x = 0.6$ on a (5×5) surface, the first 10-12 oscillations would be monolayer oscillations. At a composition of $x = 0.5$, only the first 1 or 2 oscillations would be monolayer oscillations. After the monolayer oscillations, the growth would then make a transition back to bilayer growth. Fig. 23 shows RHEED oscillations at various compositions on a (5×5) surface. Note that even at $x = 0.51$, the first oscillation is a monolayer oscillation and that as x is increased, the monolayer oscillations persisted longer. In Fig. 23 the magnitude of the oscillations generally started out small and then became larger due to the movement of the diffracted beam into the detection area of the photomultiplier. This motion was likely due to either the changing magnetic properties of the film or changing electrical transport properties as we were using direct current heating in this sample.

The results of growth on a (5×5) surface, suggest that this surface must have had excess Fe on it and this excess Fe is incorporated into growth, changing the stoichiometry of the growth front enough to cause a monolayer growth mode. If Fe incorporated only up to a saturation level around $x = 0.75$, then any Fe not incorporated into the current layer would continue to ride the surface and be incorporated into the subsequent layers. This would cause monolayer oscillations to continue until the excess Fe was used up at which point the growth mode would change to a bilayer mode. The amount of growth needed before the growth would change to a bilayer mode would be dependent on the growth composition. For the growth of $\text{Fe}_x\text{Al}_{1-x}$ with low Fe concentration, the excess Fe would be incorporated quickly and the mode would change to a bilayer mode quickly. For the growth of higher Fe concentrations, the excess Fe would be incorporated more slowly and the transition to a bilayer mode would take longer. From the measured transition times at these various coverages, we estimate that the starting surface had an excess of one half of a layer of Fe.

4.3.4 Magnetic Properties

The magnetic properties of several films were examined to see if they possessed magnetic properties that would be of interest for magnetic devices as well as to check if the films possessed the expected magnetic properties. Several samples spanning the composition range from ferromagnetic to non-magnetic were measured. Fig. 24 shows the longitudinal Kerr measurements of these samples. The longitudinal Kerr rotation is a measure of the in-plane magnetization of the film. These measurements show that the $x = 0.6$ sample was non-magnetic and the $x = 0.7$ sample had a lower saturation magnetization than the $x = 0.8$ sample, consistent with bulk measurements. The $x = 0.8$ sample showed a coercivity of about $H_c = 75$ Oe and the $x = 0.7$ sample showed a

coercivity of about $H_c = 12$ Oe. This data also indicates that the $x = 0.7$ and $x = 0.8$ sample have near 100% remanence as zero applied field. Low field measurements of the $x = 0.7$ confirmed this. From polar Kerr measurements, we found that the saturation field and maximum Kerr rotation were dependent on composition as well. For the $x = 0.8$ sample, $H_s = 16$ KOe and $\theta_k = 0.228^\circ$ whereas for $x = 0.7$ sample, $H_s = 4.5$ KOe and $\theta_k = 0.10^\circ$. Thus, simply by varying x in an epitaxial layer, one can change from ferromagnetic to non-magnetic.

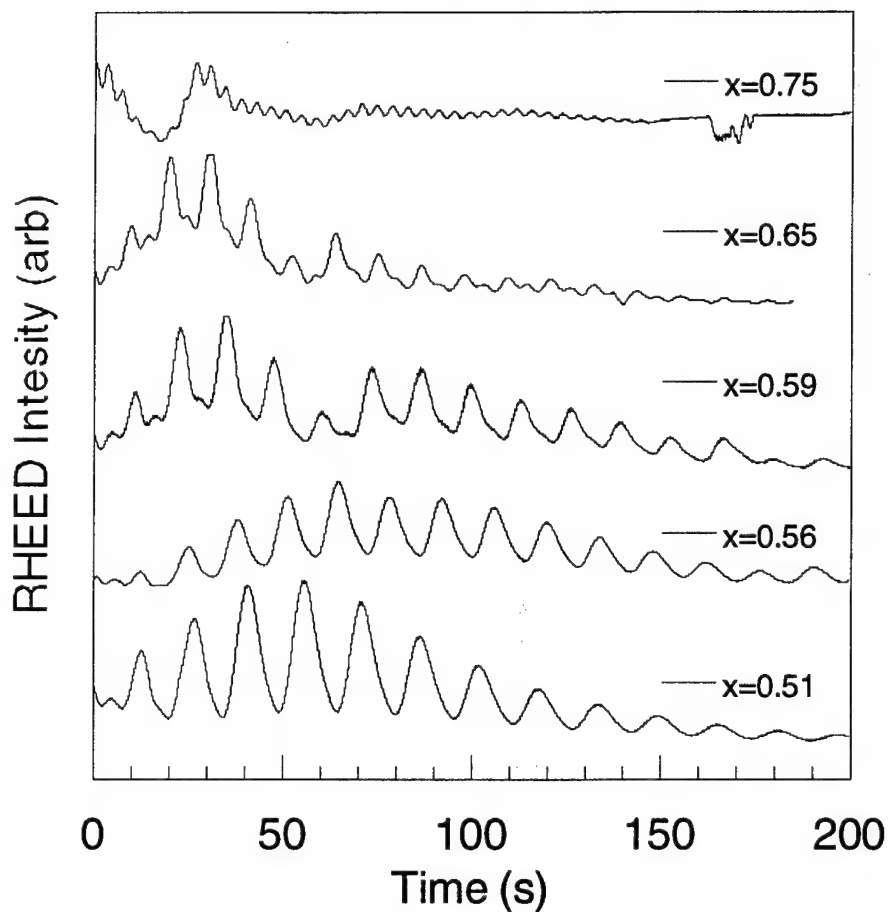


Fig. 23 RHEED oscillations due to growth on an annealed $\text{Fe}_x\text{Al}_{1-x}$ surface which exhibits a (5x5) diffraction pattern. It can be seen in that at a growth composition of $x=0.51$, the first oscillation is a monolayer oscillation and after are bilayer oscillations. At higher Fe concentrations, the monolayer oscillations last longer until above $x=0.7$ where only monolayer oscillations are observed.

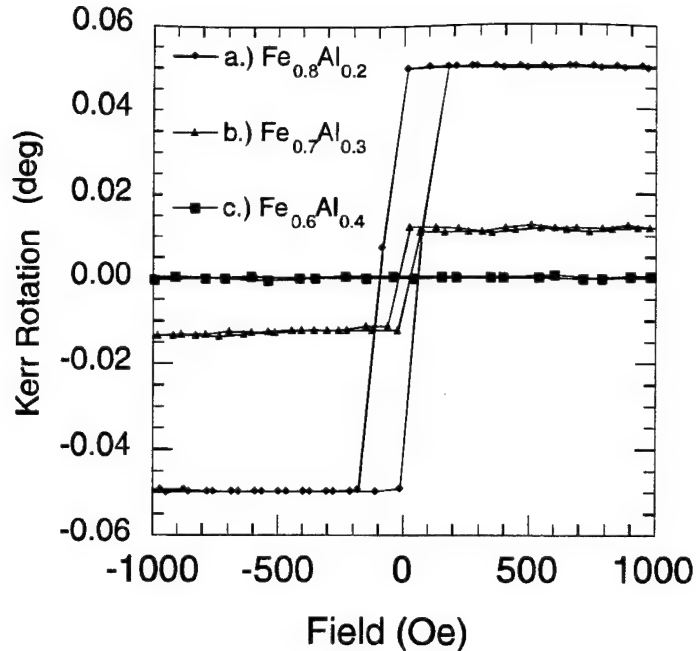


Fig. 24 Longitudinal Kerr loops of three samples of different compositions a) $x=0.8$, b) $x=0.7$ and c) $x=0.6$. The $x=0.6$ sample does not show Kerr rotation because it is non-magnetic. The other 2 samples are magnetic and show 100% in-plane remanence and a very quick magnetization reversal. The applied field at which the magnetization reverses is related to coercivity and it can be seen that the two samples have different coercivities.

4.4 Conclusion

We report on findings related to the nucleation, annealing, growth and magnetic properties of epitaxial $\text{Fe}_x\text{Al}_{1-x}$ on AlAs/GaAs. First, $\text{Fe}_x\text{Al}_{1-x}$ nucleates on an AlAs (3x2) surface in small clusters which are either amorphous or randomly oriented. Second, it is necessary to grow a minimum thickness of $\text{Fe}_x\text{Al}_{1-x}$ on AlAs at low temperatures of about 200°C before annealing in order to obtain a surface in which RHEED oscillations can be seen with continued growth. Third, the growth mode of $\text{Fe}_x\text{Al}_{1-x}$ on an annealed $\text{Fe}_x\text{Al}_{1-x}$ surface is primarily determined by growth composition. Monolayer growth occurs above $x = 0.7$ and bilayer growth occurs below that value. However, the initial growth behavior also depends upon the surface reconstruction - a (5x5) surface can force monolayer growth for at least several layers, likely due to an excess of Fe that slowly incorporates as subsequent layers are grown. Finally, samples with $x < 0.7$ were shown to be ferromagnetic with 100% in-plane magnetization. H_c , M_s and θ_k were found to be dependent on the Fe-Al ratio with all three increasing with increasing Fe concentration.

5 Growth of Hf and HfN on GaN by Molecular Beam Epitaxy

5.1 Introduction

GaN has been shown to be a technologically important material for applications in optoelectronics [45] and high temperature/high power electronic devices [46,47]. With the progress in device fabrication the need for stable high quality ohmic and Schottky barrier contacts to this material becomes especially important. Recently there have been a few reports on success in fabrication of contacts to both n- and p-type material[48-51]. However, the problem of thermal and mechanical stability of the contact materials has not been fully resolved[51,52]. Transition metals have been widely used in recent years in contacts to III-Nitrides. These include Ti/Al layers used as ohmic contacts to n-type GaN and Ni/Au layers for p-type GaN. Most of these metals have very different structures and lattice parameters than GaN. Hf and HfN are noteworthy in that they are closely lattice matched to GaN. Like GaN (Wurtzite), Hf is hcp. Their compatibility has been demonstrated by Beresford et al. who have recently reported on growth of GaN on bulk Hf substrates[53]. They have suggested that Hf has the possibility of being a compliant substrate. Further, HfN have been studied as a diffusion barrier for Al ohmic contacts on Si[54]. Because of their thermal and crystallographic compatibility, Hf and HfN epitaxial layers on GaN would offer the possibility of studying nearly ideal contacts. In this paper we report the first studies on preparing such films. Hf and HfN films were grown on GaN by molecular beam epitaxy (MBE) using NH₃. The films were studied with reflection high energy electron diffraction (RHEED) and atomic force microscopy (AFM). Based on the RHEED results, a model is proposed in which Hf grows on GaN through the formation of a HfN interface layer.

5.2 Experimental

GaN(0001) films were grown on c-plane sapphire by molecular beam epitaxy (MBE) using a Ga K-cell and an ammonia leak. The growth was conducted in a custom built system with a background pressure of 1x10⁻⁹ Torr.

Commercial, Union Carbide sapphire samples of approximately 10x11 mm in size with one side polished were cleaned in 1:1 mixture of H₂SO₄:H₃PO₄ at 65 °C for 5 min. Then, the samples were rinsed in DI water dried by nitrogen gas followed by cleaning them in acetone and methanol subsequently as described in detail by R. Held et al.[55]. To increase radiation absorption from the heater behind the sample, 50 nm of Ti followed by 200 nm of Mo were deposited on back, unpolished side of the samples in an e-beam evaporator. The samples prepared this way were then used as substrates for GaN growth. The c-plane sapphire substrate was nitrided by annealing it in an ammonia flux with a beam equivalent pressure BEP=10⁻⁵ Torr at 850 °C for 15 min. Then a low temperature GaN buffer layer was grown under conditions of excess ammonia. This procedure would produce an N polar film. GaN was then grown at 750°C, using a Ga flux of 0.3 ML/s and an NH₃ BEP of 5x10⁻⁶ Torr. GaN(0001) films with thicknesses between 0.6-1.8 micron were grown. RHEED was used to determine the Ga condensation temperature and further GaN growth monitoring[55]. The surface was then annealed in ammonia as the temperature lowered to room temperature. The films had relatively streaky, 2D RHEED patterns and possessed an rms roughness of less than 1nm as determined by AFM. These films were used as substrates for subsequent Hf and HfN growth, without exposure to the atmosphere.

Hf was deposited in the MBE chamber using a custom built, Jonker-style electron beam source [43] that was surrounded by a liquid nitrogen cryoshroud. A cylindrical Hf rod (3N purity) was used as a source material. Biased at +7 kV the Hf piece is selectively

heated by the electrons emitted from a circular tungsten filament. The Hf source was operated at about 150 W to achieve a deposition rate of up to 30 nm per hour. Hf was deposited on top of GaN at the temperatures between 20°C and 730°C both with and without ammonia in the system. RHEED studies of GaN and Hf films have been conducted using a Physical Electronics Industries 10 kV electron gun, and custom built octupole electrostatic deflectors.

5.3 Results

Hf was deposited on the GaN films as described in Section 5.2. Initially transmission features in the diffraction pattern were observed; after about 100 nm of deposition the pattern showed more of a 2D, streak character, as shown in Fig. 25. The film was epitaxial with the underlying GaN surface, and the measured separation between the streaks repeated every 60°, as expected for the hexagonal lattice. Also, the Hf RHEED pattern was found to be rotated by 30° with respect to that of the underlying GaN. The lattice parameter of Hf is very close to GaN. But the separations of the diffracted beams parallel to the surface in the 30° pattern from GaN is 1.43 times the separation of the Hf 0° pattern. This suggests a root 2 by root 2 R30° surface reconstruction.

Atomic force microscopy was used to examine the surface morphology of the Hf films. A 5 μm area scan presented in Fig. 26. indicates a rough film surface consisting of hills with a step and terrace structure. A 1 μm scan of the plateau area is presented in Fig. 27. It shows that the growth of the Hf film occurs by a hillock mechanism, though the nucleation process of Hf on GaN is yet to be studied. The surface of the film contains macrosteps with the average height of 10 nm. An rms roughness of the plateau areas is found to be of the order of 3.2 nm. The step edges show some pinning; no clearly defined screws can be resolved.

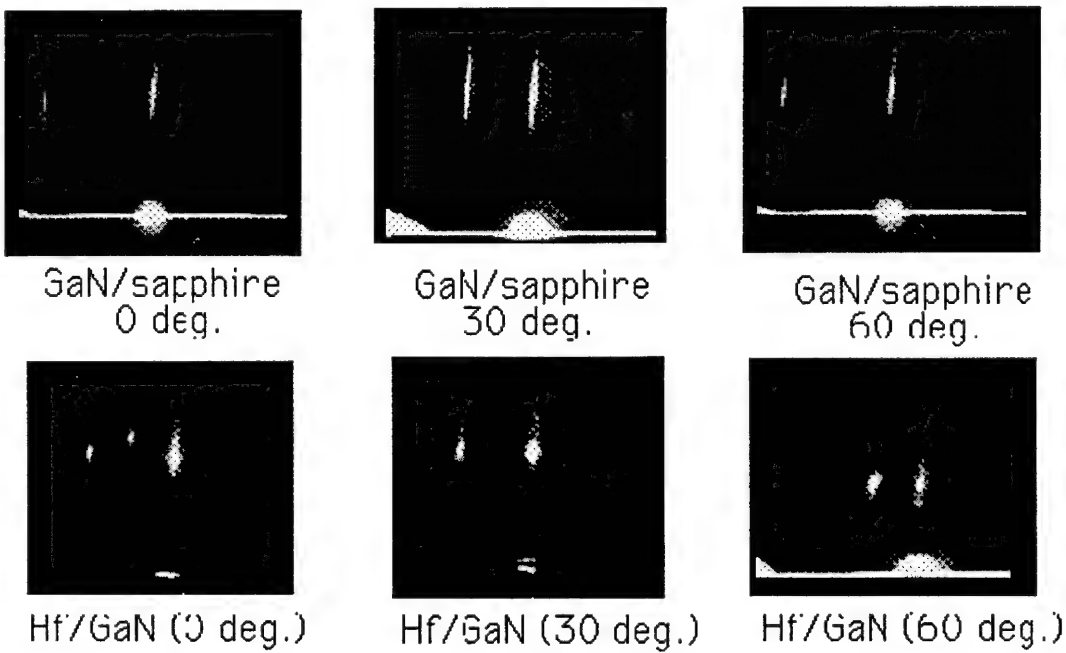


Fig. 25 RHEED patterns of GaN substrate and 100 nm thick Hf film grown on this substrate.

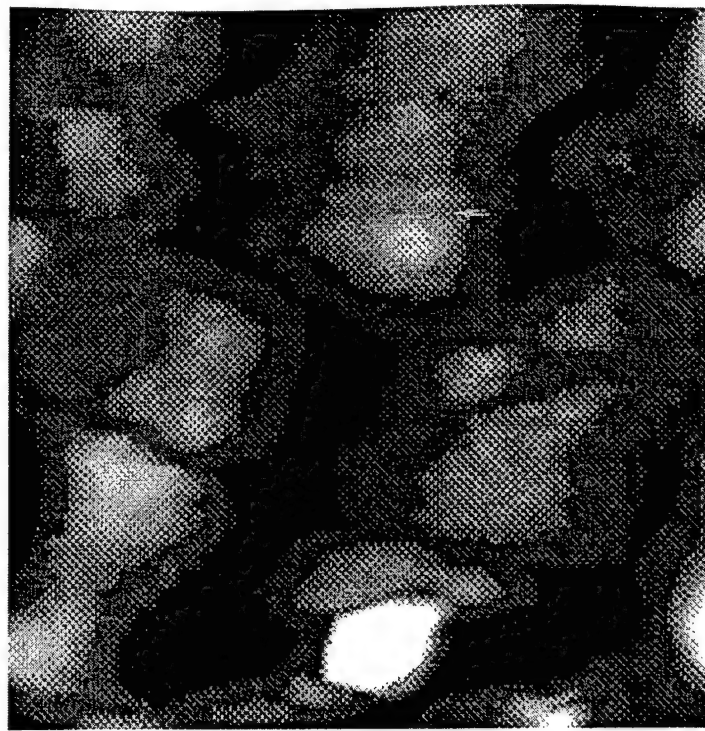


Fig. 26 AFM image of 5 μm area of 100 nm thick Hf film grown on GaN at room temperature

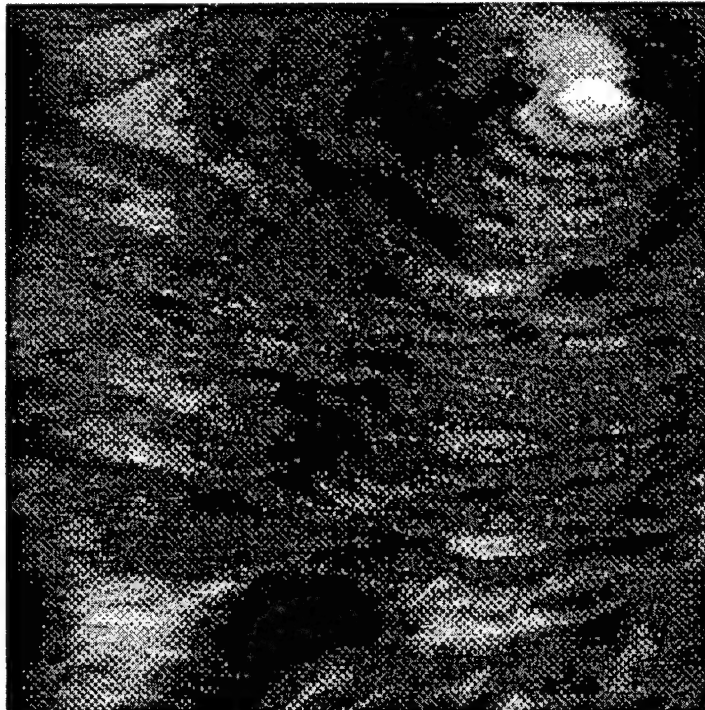


Fig. 27 AFM image of 1 μm area of 100 nm thick Hf film grown on GaN at room temperature. The macrosteps in the figure have a mean height of 10 nm.

When the Hf films were annealed in vacuum at temperatures up to 700°C, a change to a transmission diffraction pattern was observed. If Hf was deposited at NH₃, BEP= 10⁻⁷ Torr and substrate temperatures above 350°C, a diffraction pattern consisting of arcs and corresponding to that of a polycrystalline material was observed. AFM found these to have an rms roughness of up to 40 nm for a 100 nm film. Auger Electron Spectroscopy (AES) indicated the Hf:N ratio in these films is roughly stoichiometric HfN.

5.4 Discussion

Both Hf and HfN are well lattice matched to GaN can be seen in the data listed for reference in Table 1.

Material	Structure	Lattice Parameter (Å, R.T.)	Melting Point
GaN	Wurtzite	a=3.19 c=5.19	800°C decomposition
Hf	HCP	a=3.19 c=5.04	2231°C
HfN	NaCl	a=4.52	3305°C

Table 1 Selected properties of GaN, Hf, and HfN.

As a group IVB element, Hf is predicted to be thermodynamically unstable on GaN[56]. Theoretical studies of the Hf-Ga-N ternary system indicated that HfN phase forms a tie-line with GaN while pure Hf does not[56]. Hence we expected that for pure Hf deposition onto GaN it would have been more difficult to obtain a smooth, unreacted interface than with HfN. However, at the temperatures required for HfN deposition this was not the case. Smoother films could ultimately be grown with Hf alone.

The RHEED data of Fig. 25 indicate a 30° rotation within the c-plane of Hf grown on GaN at room temperature. To see this examine the Ewald construction of Fig. 28. In this RHEED geometry the Ewald sphere is nearly tangent to the reciprocal lattice rods and so it is easiest to imagine a plane rather than a sphere as the locus of the allowed diffracted beams. Viewing the surface reciprocal lattice rods from above, the construction consists of a line perpendicular to the incident beam superimposed on the reciprocal lattice. The points of intersection are the allowed beams. In Fig. 28 three lines are drawn, corresponding to the planes perpendicular to the three incident directions in Fig. 25. In the construction, the circles correspond to the reciprocal lattice rods of GaN and the crosses correspond to that of Hf, taken from Fig. 25. Because the electron beam cannot penetrate the Hf overlayer, both patterns are not seen together. The rotation, by itself, is apparent because, for example, the 0° pattern of GaN shows the beams with their largest separation, while for Hf, the beams are at their closest separation. The ratio of the streak separations in the 30° pattern and the 0° pattern is 1.43. Together we conclude that, with perhaps a 2% expansion, the Hf surface has a root 2 by root 2 R30° reconstruction. Previously, Beresford [53] observed bulk crystalline Hf(0001) surfaces that were prepared by a sputter and anneal cycle that did not show this reconstruction. In their procedure, however, hydrogen was not used and so, as for other metal surfaces, H adsorption might induce the reconstruction we observe.

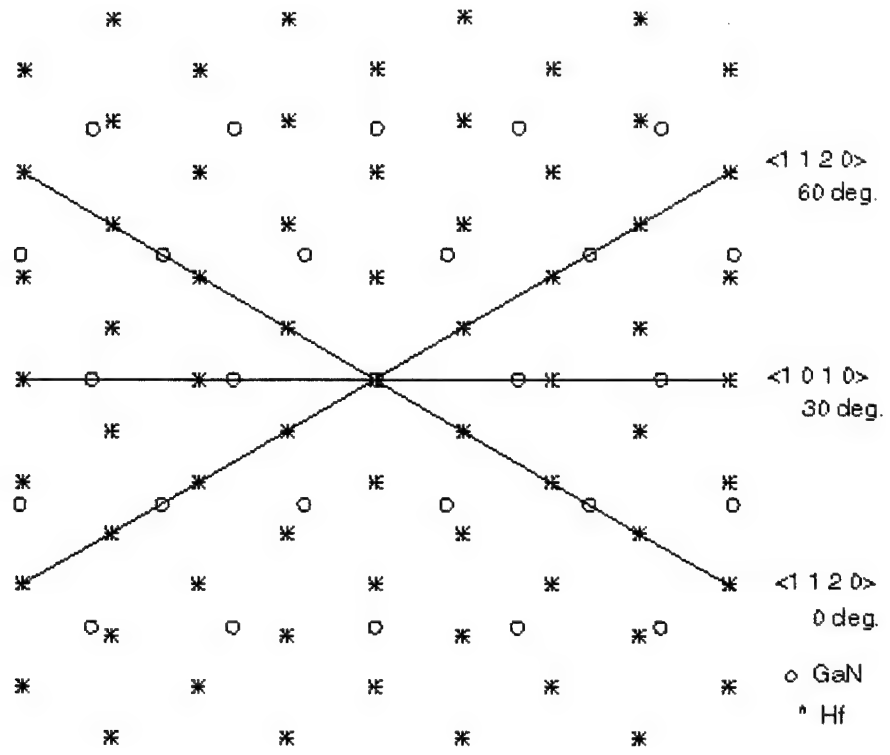


Fig. 28 Model of reconstruction

We suggest that the 30° rotation is due to reaction at the GaN/Hf interface. To explain this model consider certain structural properties of Hf, HfN, and GaN as presented in Table 1. GaN has a Wurtzite structure with an atomic layer stacking sequence along the c-axis corresponding to that of the hexagonal close-packed (hcp) structure with two atoms per basis. Such a periodicity can be represented as ABAB... where atoms of each sublattice in GaN move from position A to position B as depicted in Fig. 29b.

If there were no interfacial reaction, Hf, which also has an hcp structure and which is lattice matched to GaN, would grow with the original substrate stacking sequence resulting in an unchanged RHEED pattern. Instead, Hf reacts with GaN at the interface forming HfN that has a sodium chloride structure with the atomic layer sequence along the close-packed direction of ABCABC... as shown in Fig. 29a. The formation of the HfN(111) at the interface changes the GaN stacking sequence to that of a cubic HfN that further changes again to that of the hcp Hf as more material is grown. Such changes in the atomic layer stacking sequence that can be represented as ABAB... C...ACAC...(Fig. 29c) cause a 30° rotation in the c-plane, as seen with RHEED. This type of rotation could occur in the middle of a flat terrace on a GaN surface; it could also happen at a step edge. The latter would limit the formation of domain boundaries in the Hf overlayer.

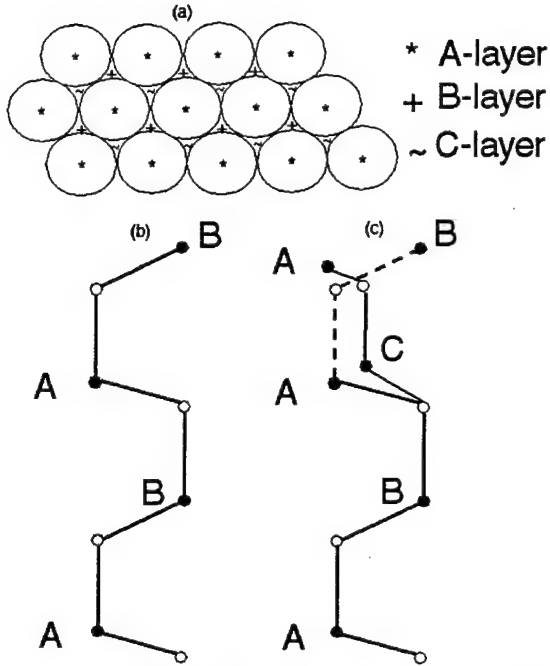


Fig. 29 Model of Hf growth on GaN through the formation of the HfN interface layer:
 (a) Atomic positions in the cubic close-packed structure; (b) stacking sequence along c-axis in Wurtzite GaN; (c) change in the stacking sequence along c-axis caused by the formation of the cubic close-packed phase

5.5 Summary

Hf has been epitaxially grown on GaN at room temperature. RHEED indicated that Hf grows on GaN with a 30° rotation in the c-plane. This change in the RHEED pattern can occur due to the formation of a cubic HfN interface layer that introduces a rotation in the Hf structure with respect to the underlying GaN. Also, the RHEED data shows that the Hf surface is root 2 by root 2 R30° reconstructed, perhaps caused by the residual hydrogen in the system. Since smooth Hf films can be grown, they might serve as compliant substrates for subsequent GaN growth or for metal semiconductor superlattices.

6 Atomic Level Characterization of Epitaxial Grown Metallic Compounds on III-V Semiconductors

We have established MBE growth procedures for growing high quality rare-earth arsenides (RE-As), which have the NaCl crystal structure, and transition metal-group-III (TM-III) compounds with the CsCl crystal structure on zincblende III-V semiconductors ($\text{Ga}_{1-x}\text{Al}_x\text{As}$ and $\text{Ga}_{1-x}\text{In}_x\text{As}$)[15,36,57-67]. During this project, we have been able to obtain atomic resolution images of the surfaces of both $\text{Sc}_{1-x}\text{Er}_x\text{As}$ (Fig. 30) and CoGa grown on GaAs in addition to $\text{Fe}_{1-x}\text{Al}_{1-x}$ and HfN (discussed in sections 3 and 4, respectively) by Scanning Tunneling Microscopy (STM). The STM image in Fig. 30 was obtained by As-capping the as-grown ErAs in one MBE system, transporting through air and decapping the As in the STM system. In the case of $\text{Sc}_{1-x}\text{Er}_x\text{As}$ growth, monolayer thick islands ~150 Å diameter are clearly evident. Although there is no strong asymmetry of the island shapes, there is about a 1 monolayer buildup of material on the top of substrate step edges, which indicates the existence of a Schwoebel barrier at the step edge.



Fig. 30 100nm x 100nm STM image of ErAs/GaAs(100).

7 Semiconductor Growth on Metallic Compound Layers

Growth of high quality III-V semiconductors on top of metallic compounds has proved to be difficult[15,36]. This arises from differences in bonding, relative surface energies and crystal structures of the metallic compounds and III-V semiconductors. In order for the compound metal layer to grow in a layer-by-layer fashion on the compound semiconductor surface, its surface energy plus the interface energy must be lower than the surface energy of the compound semiconductor. Similarly, for the compound semiconductor to grow in a layer-by-layer fashion on the metallic compound surface, its surface energy plus the interface energy must be lower than the surface energy of the metallic compound. Clearly, both these criteria cannot be met normally. From thermodynamics, the only way to achieve this III-V/M/III-V structure would be to modify the surface or interface energies during the growth. In the past we had found that by growing on different crystallographic orientations, the relative surface and interface energies could be adjusted to improve the GaAs wetting of $\text{Sc}_{1-x}\text{Er}_x\text{As}$ surfaces[36]. The optimum orientation was found to be {311}. During the current research we developed an interlayer bonding model to explain the effects of adding interlayers in the growth of GaAs on ErAs.

7.1 Controlling Semiconductor Overgrowth Through the use of a Bond Tailoring Interlayer (interface energy modification)

A key to enable high quality overgrowth is to tailor the bonding between the metallic compound and growing semiconductor. Both the crystal structure and bonding are dissimilar in the metallic compounds and the semiconductor. In the case of RE-As and RE-N compounds, the crystal structure is NaCl and the bonding ionic. For III-V semiconductors, the crystal structure is zincblende or wurtzite structure and the bonding is primarily covalent. For growth of semiconductors on (100) $\text{Sc}_{1-x}\text{Er}_x\text{As}$, increasing the degree of ionicity of the semiconductor improved the overgrowth. Ge, a covalently bonded semiconductor, would not wet the (100) $\text{Sc}_{1-x}\text{Er}_x\text{As}$ surface. Amorphous Ge layers deposited at room temperature were found to dewet the surface, forming spherical crystalline islands, when the structures were heated to recrystallize the Ge by solid phase epitaxy. We investigated bonding interlayers to account for the differences in bonding between the semiconductor and metallic compound layers.

Previously we found that one monolayer of Mn deposited prior to GaAs overgrowth on ErAs improves the wetting[68]. Secondary ion mass spectrometry sputter >depth profiles indicate that the Mn remains at the GaAs/ErAs interface, suggesting that the Mn is acting as an interlayer rather than a surfactant layer that would ride continuously on the GaAs surface during growth. Hence, a model was developed to explain the Mn behavior, which we consider to be a bond-angle-tailoring model. In the

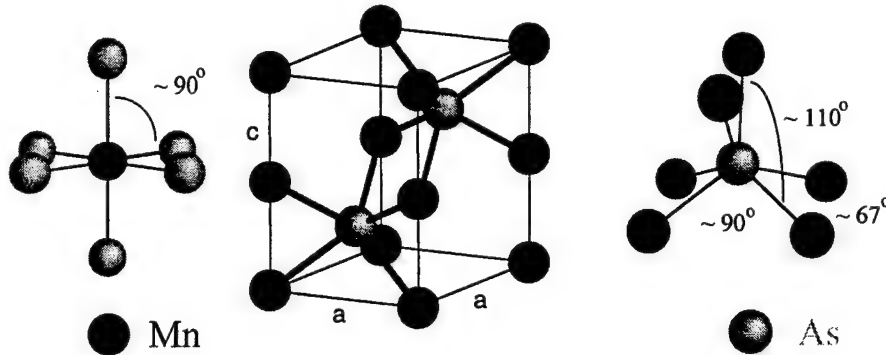


Fig. 31 MnAs crystal structure (NiAs type). The inserts show the atomic coordination around the Mn and As atoms respectively.

model, the detailed bonding of the interlayer is key. MnAs has the NiAs crystal structure shown in Fig. 31. Investigation of the MnAs crystal structure reveals that the Mn coordination is virtually identical to the Er coordination in ErAs (insert in Fig. 31). The As, on the other hand, has a coordination in between that of As in ErAs and GaAs (insert in Fig. 31). This is what allows MnAs to act as the bond tailoring interlayer. MnAs grows with $(1102)\text{MnAs} \parallel (100)\text{ErAs}$ [68]. In this orientation, Mn and As form zig-zag chains on the surface (Fig. 32). If these Mn atoms are replaced by Ga, the Ga chains formed will have bond angles closer to that found for Ga in GaAs as the Ga-As bond length is slightly shorter than the Mn-As bond length, making the Ga atoms move down and increase the bond angle from ~92° towards ~109° found in GaAs (Fig. 33). The Ga atoms in the

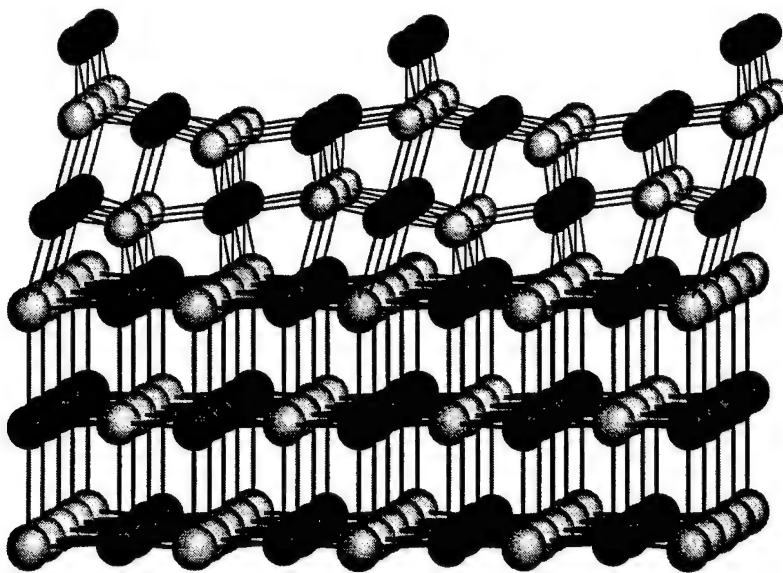


Fig. 32 Schematic of a possible $(\bar{1}102)\text{MnAs}||(100)\text{Sc}_{1-x}\text{Er}_x\text{As}$ heterostructure atomic alignment.

chains are believed to act as nucleation sites for further GaAs growth. A difference in the interface structure between ErAs grown directly on GaAs and GaAs grown on ErAs with 1 ML MnAs can be seen in the high resolution cross-sectional TEM micrograph shown in Fig. 34. Unfortunately, detailed image simulations have yet to be done to determine if the top interface structure corresponds to that proposed above.

Lattice mismatch is an issue. For this $<\bar{1}\bar{1}20>(\bar{1}102)\text{MnAs}||<011>(100)\text{Sc}_{0.3}\text{Er}_{0.7}\text{As}$ alignment, the mismatch is -7% along $<011>\text{ Sc}_{0.3}\text{Er}_{0.7}\text{As}$ and 7.6% along $<0\bar{1}1>\text{ Sc}_{0.3}\text{Er}_{0.7}\text{As}$ for a coincidence of 1 MnAs to 2 $\text{Sc}_{0.3}\text{Er}_{0.7}\text{As}$ surface unit cells. This large a mismatch may explain why the thickness of the MnAs layer is found to be critical. Better lattice matching may be achieved with other interlayers with the same crystal structure.

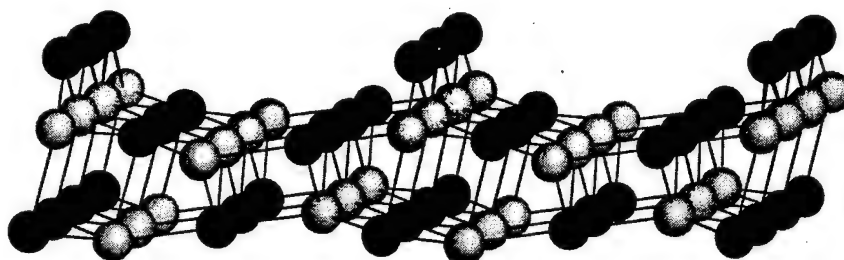


Fig. 33 Schematic of Ga absorption on $(\bar{1}102)\text{MnAs}$ showing the possible formation of anchor points for GaAs nucleation formed by the Ga atoms replacing Mn atoms on the $(\bar{1}102)$ surface.

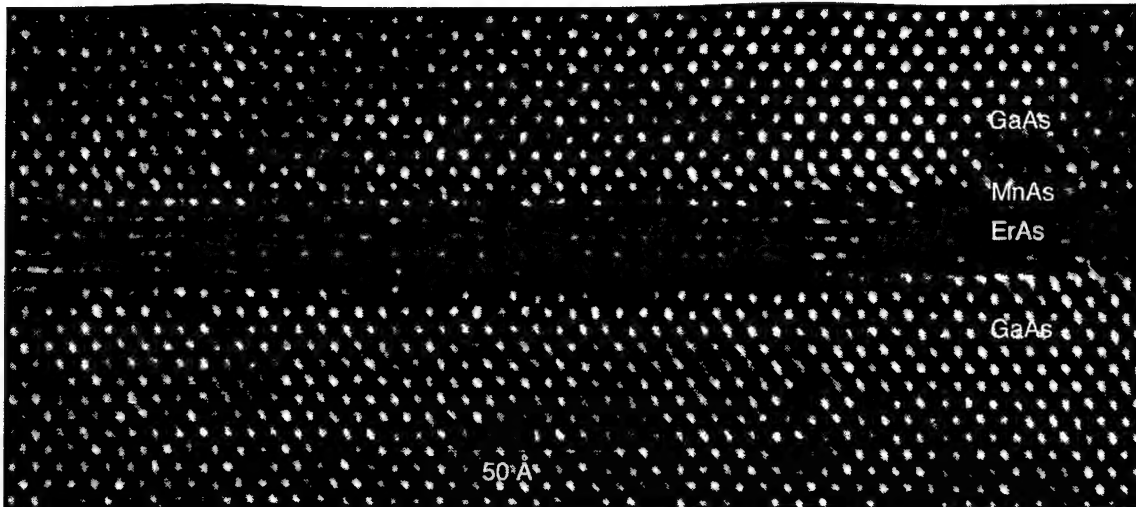


Fig. 34 High resolution TEM cross-section of a GaAs/MnAs/ErAs/GaAs(100) heterostructure. Note the difference in the interface structure of the top and bottom GaAs/ErAs interface.

8 Magnetotransport in Metallic Compound/Semiconductor Heterostructures

In collaboration with Jim Allen's group at the University of California, Santa Barbara, we have been investigating the magnetotransport of ErAs/Ga_{1-x}Al_xAs heterostructures. This involved resonant tunneling through ErAs semimetal quantum wells[69,70] and giant magnetoresistance measurements of nanocomposites of ErAs clusters in GaAs[71]. For the resonant tunneling devices, schematically shown in Fig. 6, the growth was performed on (311) surfaces as these yielded the highest crystalline quality heterostructures. Two different resonant channels were observed. The magnetic field dependence is different for the two. The channel assigned to the light hole splits into two channels for a perpendicular applied magnetic field, whereas the heavy hole resonance increases with an in-plane applied magnetic field (Fig. 35). The assignment to the light and heavy holes was made from the variations in energy for the resonant channels with thickness of the ErAs film. Fig. 36 shows the ErAs band structure calculated by Petukhov et al.[72] and the dispersion of the resonant tunneling channels ($k=1/t$, where t is the ErAs film thickness). The data points are the experimental measurements and the lines are the band structure calculations[73] in the <311> direction. There is qualitative good agreement between theory and experiment.

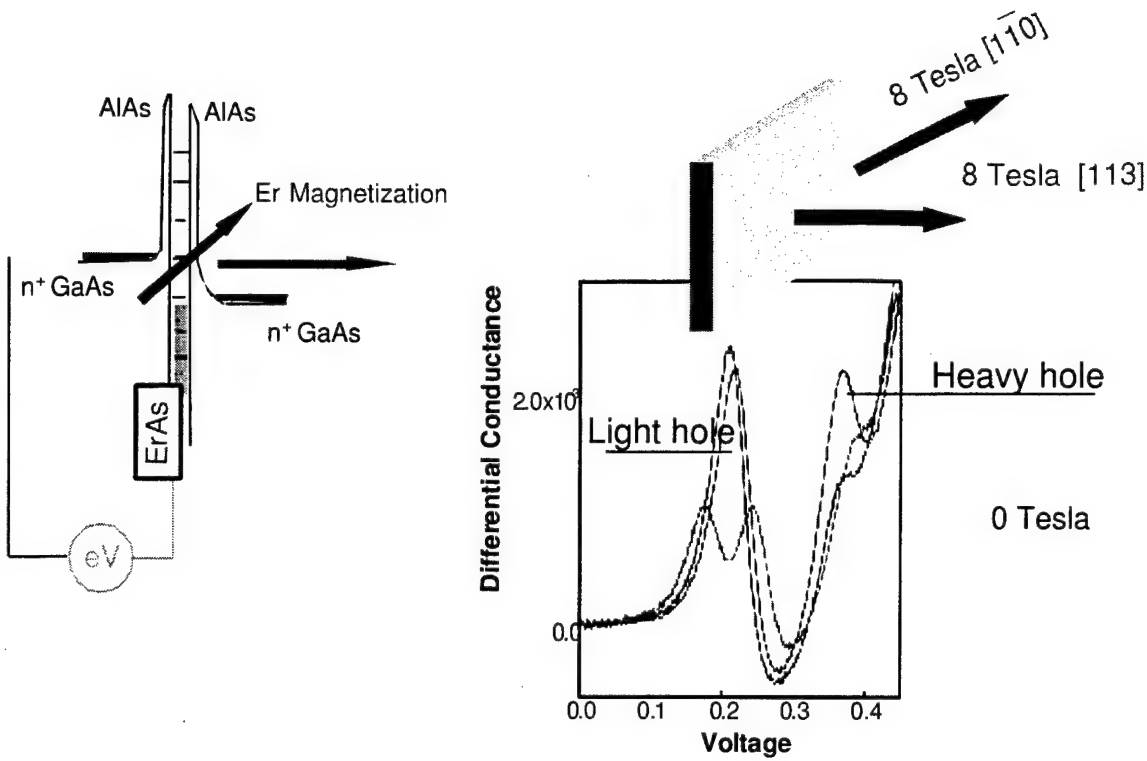


Fig. 35 Schematic of GaAs/AlAs/ErAs/AlAs/GaAs resonant tunnel diode structure together with the differential conductance showing two different resonant channels.

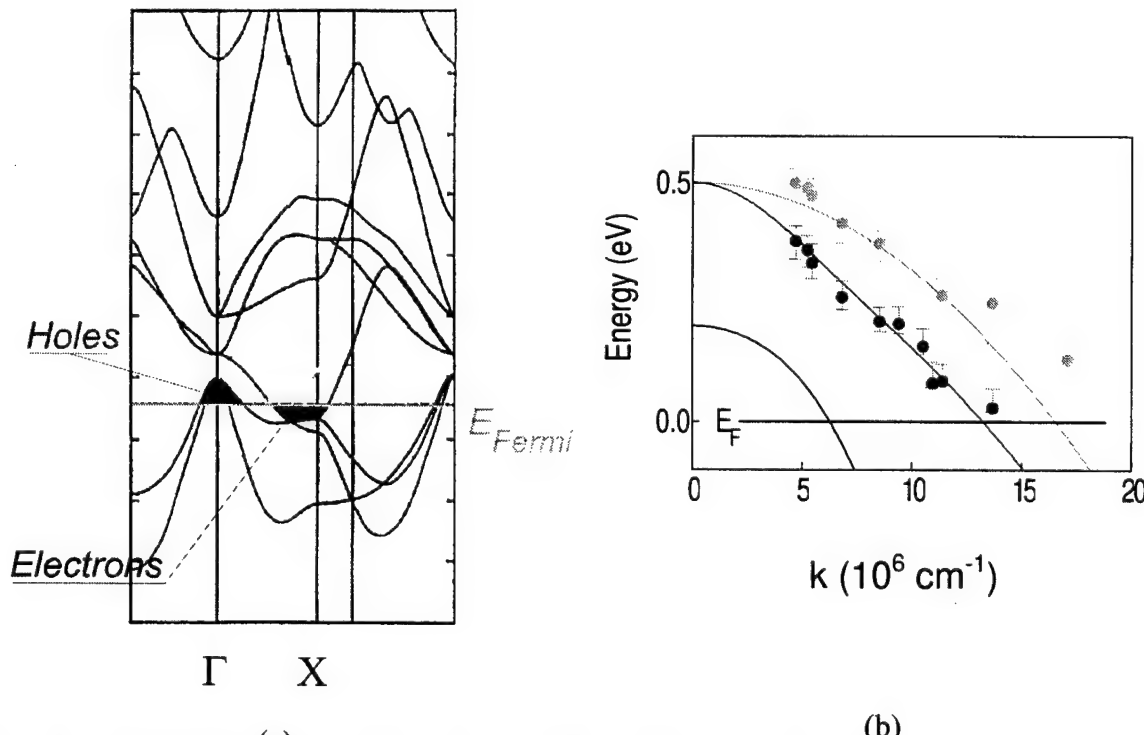


Fig. 36 (a) Band structure of ErAs[72] and (b) the dispersion of the hole channels (points) and the calculated hole band structure in the <311> direction[73].

9 Growth Rate Reduction of GaN Due to Ga Surface Accumulation

9.1 Introduction

A number of issues related to growth kinetics of GaN must be addressed. Historically, the n-type conductivity commonly exhibited by GaN was attributed to N vacancies [74]. This problem was thought to arise from a kinetic barrier to N incorporation during growth. Recent results by Lee et. al [75] and also by Jones et. al [76] using NH₃ as the nitrogen precursor during molecular beam epitaxy (MBE) indicate that the GaN growth rate is strongly temperature dependent, exhibiting a maximum between 750°C and 800°C. The high temperature decrease in growth rate is typical of GaN, and has been attributed to Ga desorption at elevated substrate temperature [75] [76] as well as to the decomposition of GaN [77]. At lower substrate temperature the common belief is that reduced N incorporation efficiency limits the growth rate [75].

In this report we will address the low temperature issues related to GaN MBE where the GaN decomposition rate is much less than the growth rate. In the results section we examine the transient response of the GaN surface composition and chemistry to a step-function of Ga flux. The time dependence of the Ga desorption after exposure of the surface to incident Ga indicates that Ga adsorbs to the surface in two states. The first deposited layer of Ga sticks to the surface in a strongly bound state, whereas subsequent desorption occurs at a higher rate. The more tightly bound of these layers is observed only when the surface has been previously exposed to NH₃.

In the results section we further examine the relationship between growth rate, substrate temperature and the incident fluxes. We show how desorption mass spectroscopy (DMS) can be used to determine whether the GaN formation rate is limited by the available N (Ga rich) or by the available Ga (N rich) and present a single rate equation to explain a decrease in the GaN formation rate with increasing Ga flux.

9.2 Experimental

Growth was carried out in a cryopumped Gen II MBE system which is shown schematically in Fig. 37. A quadrupole mass spectrometer mounted in one of the source ports enabled detection of the type and intensity of desorbed species from the substrate surface. The specular RHEED intensity was monitored using a photomultiplier tube. The NH₃ flux was held constant during growth using a capacitance manometer in conjunction with a closed loop PID controller and solenoid control valve to maintain constant pressure in the NH₃ gas line behind a manually regulated precision leak valve. A flux monitor located on the back of the sample manipulator was used to determine the incident beam equivalent pressure by rotating the sample manipulator. Absolute calibration of the incident Ga flux is achieved by monitoring RHEED intensity oscillations during growth of GaAs(001) in a separate experiment.

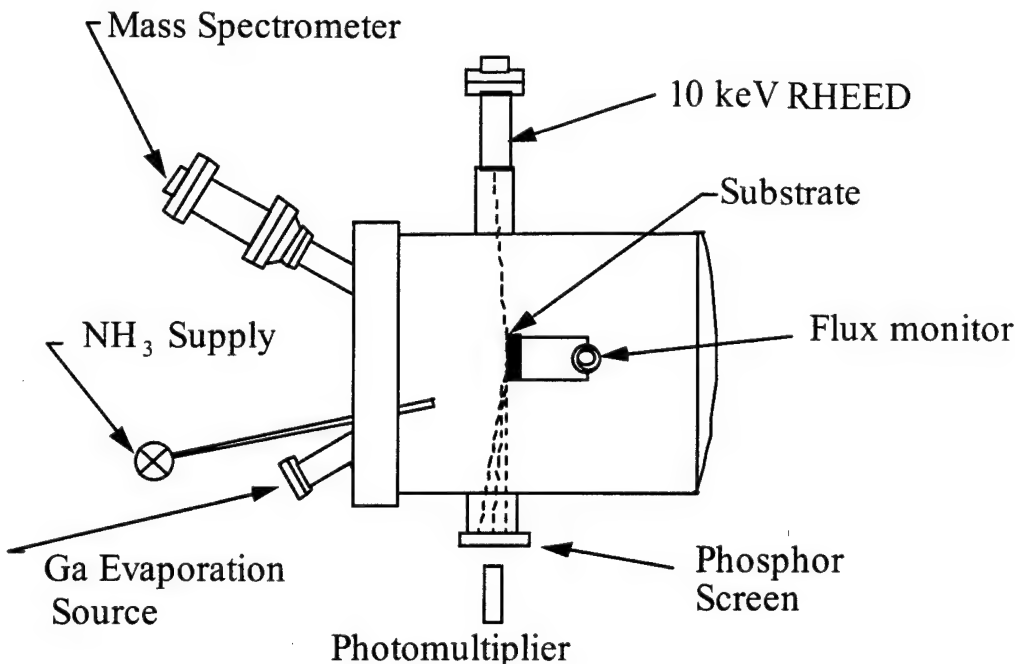


Fig. 37 Schematic diagram of the Gen II MBE system used for growth.

Samples were prepared by successively cleaning in acetone and methanol, which was followed by a 5 minute etch at 70 C in 3:1 $H_3PO_4:H_2SO_4$. The substrates were then rinsed in deionized water and blown dry with N₂. This process resulted in atomically smooth surfaces that exhibited 100 nm terraces as indicated by atomic force microscopy (AFM). Without the etch, AFM showed polish marks on the substrate surface, and no atomic steps could be seen.

The samples were loosely mounted via mechanical support in order to reduce thermal stress during growth. Consequently, thermal contact between the substrate heater and the sample was reduced, and a 0.2 μm layer of Ti was deposited on the back of the wafers to efficiently couple radiative energy from the heater to the substrate.

9.3 Results

9.3.1 Transient Response of the Surface Composition

The transient response of the specular RHEED intensity observed along the <0112> azimuth as well as the response of the desorbed Ga and H₂ fluxes to a step-function of incident Ga on the GaN surface are shown in Fig. 38. These data were measured after growth had been terminated and the background NH₃ pressure had been reduced to <10⁻⁹ Torr while maintaining a constant substrate temperature of 760°C. A number of important features are observed after opening the Ga shutter. The initially low Ga desorption flux seen in Fig. 38 indicates that Ga adsorbs in a strongly bound site that is characterized by a long residence time. We also see in Fig. 38 that H₂ is a byproduct of this adsorption process. After deposition of roughly one monolayer, the Ga desorption increases and the H₂ desorption decreases, indicating the presence of a second, weakly bound state. These results are consistent with the findings of Jones et. al [76] and Lee et. al [75] who both proposed that Ga exists in two adsorption sites during growth. After this

initial Ga pulse, we close the Ga shutter and allow the excess Ga to desorb from the surface. Subsequent exposure to incident Ga results in only the higher Ga desorption flux, with no detectable change in the H₂ desorption, and no reduced desorption flux indicative of the strongly bound Ga. We can again prepare a surface that will adsorb Ga in the strongly bound sites by exposing the surface to NH₃. The procedure outlined above can be used to detect the presence of these sites.

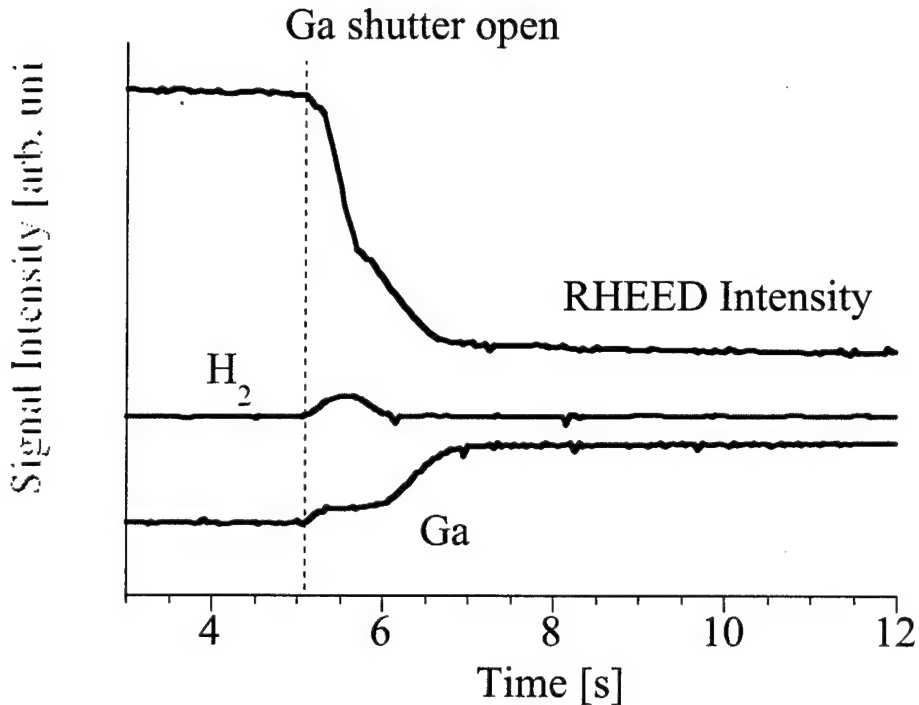


Fig. 38 The transient response of the Ga and H₂ desorption to a step-function of incident Ga is shown in the absence of incident NH₃. The response of the specular RHEED intensity observed along the <0112> azimuth is also shown. ($F_{\text{Ga}} = 1.6 \times 10^{15} \text{ cm}^{-2} \text{ s}^{-1}$, $T_{\text{sub}} = 760^\circ\text{C}$).

Measurement of the RHEED intensity as shown in Fig. 38 and Fig. 39 reveals that two slope maxima occur during the initial transient RHEED decrease. Quantitative information can be extracted from this RHEED intensity variation by definition of the time interval, t , as shown in Fig. 39. We find that the time dependence of the transient Ga and H₂ desorption track this RHEED intensity variation as indicated in Fig. 38. Based on this observation we believe that t gives an estimate of the time required for saturation of the strongly bound Ga sites. The quantity $1/t$ decreases linearly with increasing NH₃ beam equivalent pressure (BEP), while it increases linearly with incident Ga flux. Furthermore, this behavior is observed only when the incident Ga exceeds the available N provided by the incident NH₃.

Based on these transient data, we have identified two Ga adsorption sites. We will present evidence in the next section that the more tightly bound Ga site contributes to

growth, whereas the weakly bound Ga acts to inhibit growth by blocking the strongly bound Ga, and inhibiting the incorporation of N from NH_3 .

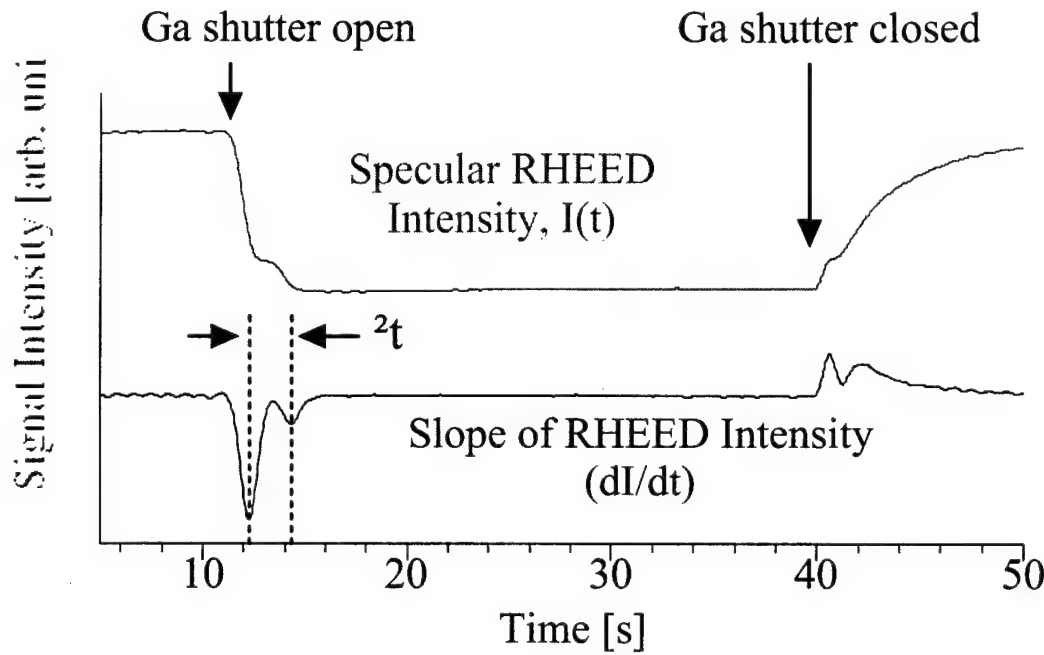


Fig. 39. Specular RHEED intensity and its first derivative. Differentiation of the signal allows quantitative analysis of the transient signal. Experimental conditions for the data shown here are $T_{\text{sub}}=780^\circ\text{C}$, NH_3 BEP= 1.1×10^{-5} torr, $F_{\text{Ga}} = 1.45 \text{ML/s}$.

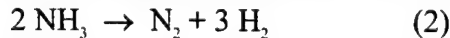
9.3.2 Steady State Growth Behavior

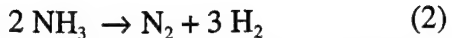
RHEED indicates that high Ga flux and high substrate temperature are necessary to achieve atomically smooth surface morphology. The objective of this section is to examine the growth kinetics when the incident Ga exceeds the available N provided by NH_3 .

In Fig. 40 and Fig. 41 we see the desorbed H_2 , N_2 , and Ga fluxes resulting from exposure of the GaN surface to a 15 second pulse of Ga while the NH_3 BEP is held constant. For the data shown in Fig. 40 the Ga flux was $4.2 \times 10^{14} \text{ cm}^{-2}\text{s}^{-1}$ whereas in Fig. 41 it was increased to $1.4 \times 10^{15} \text{ cm}^{-2}\text{s}^{-1}$. All other growth parameters were the same for both plots. The increased H_2 desorption during growth is attributed to the forward reaction



In the absence of incident Ga we find that contributions from the reaction





become significant at substrate temperatures exceeding 800°C, and we have not yet determined the relative contributions of the two reactions during and prior to growth at elevated temperatures. At temperatures below 800°C, however, we believe that H₂ yields a reliable estimate of the growth rate. The accuracy of this technique is currently being investigated using post growth film thickness measurements.

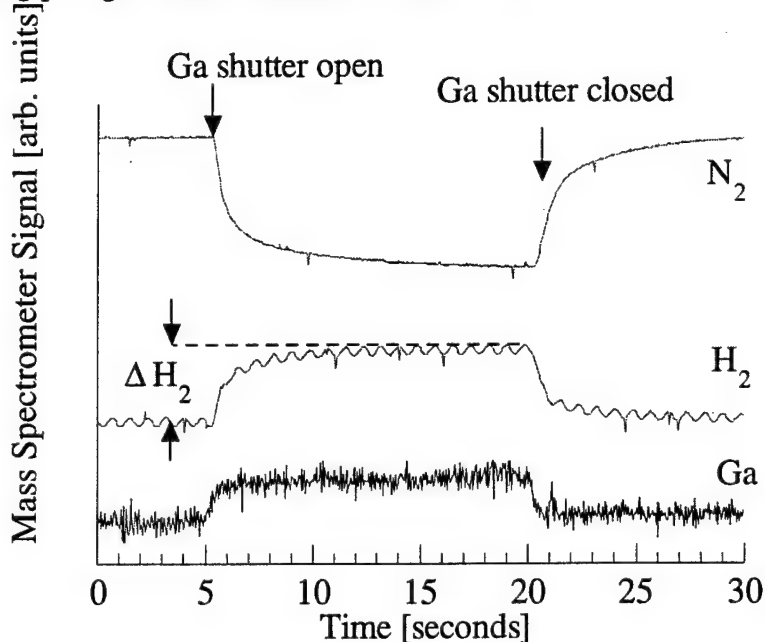


Fig. 40 Changes in the N₂, H₂ and Ga desorption are caused by exposing a smooth GaN sample to a 15 second pulse of incident Ga under N rich growth conditions. Substrate temperature=820°C, NH₃ beam equivalent pressure = 7×10^{-6} torr, Ga flux = $4.2 \times 10^{14} \text{ cm}^{-2}\text{s}^{-1}$. The high frequency H₂ signal oscillations arise from fluctuations in H₂ background pressure caused by temperature cycling of the cryopumps.

In Fig. 41 we see that initiation of growth causes a transient pulse of H₂ to desorb from the surface, whereas in Fig. 40 the desorbed H₂ flux reaches its maximum value at steady-state. In general, we find that the desorbed H₂ flux during steady-state growth increases linearly with increasing Ga flux, but then decreases as the Ga flux exceeds a saturation value. This relationship is shown in Figure 6, where we see the dependence of H₂ on the incident Ga flux at three different substrate temperatures.

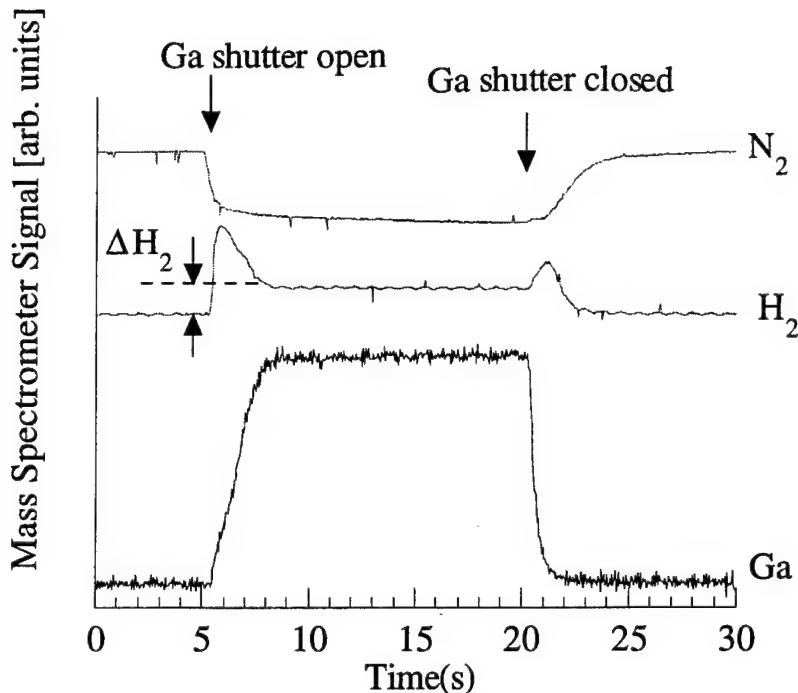


Fig. 41 Changes in the N_2 , H_2 and Ga desorption are caused by exposing a smooth GaN sample to a 15 second pulse of incident Ga under Ga rich growth conditions. Substrate temperature=820°C, NH_3 beam equivalent pressure = 7×10^{-6} torr, Ga flux = $1.4 \times 10^{15} \text{ cm}^{-2}\text{s}^{-1}$. The H_2 signal oscillations arise from fluctuations in H_2 background pressure caused by temperature cycling of the cryopumps.

In Fig. 42 we see that high Ga flux causes a reduction in the growth rate, but that increasing the substrate temperature minimizes this effect. As mentioned previously, a temperature gradient of about 20°C exists across the substrate. This gradient introduces uncertainty to the data shown in Fig. 42, since DMS measurements integrate the desorbed flux over the whole sample. The effect is particularly pronounced at high incident Ga flux, where the growth rate is strongly temperature dependent. This problem also makes verification of the DMS data difficult, since film thickness measurements are dependent on the location on the sample where the film thickness is measured. These difficulties can be overcome by conducting the same measurements on samples that are known to be isothermal, and work is currently underway to achieve.

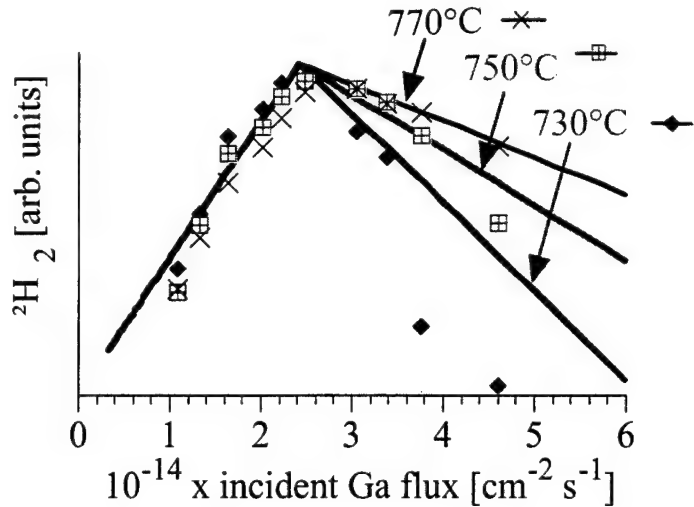


Fig. 42. Dependence of H_2 on the incident Ga flux. The lines show the theoretical incorporation rate based on the simple kinetic model presented in this paper.

In spite of the problems introduced by the temperature gradient, we are confident that the data in Fig. 42 yield an accurate picture of the general dependencies between growth rate, fluxes, and substrate temperature. The reduced growth rate at high Ga flux can be accounted for by consideration of the following simple kinetic model. We start by making a number of assumptions about the atomistic behavior of adsorbed Ga which will be justified by agreement with measured data. First, based on the DMS measurements we consider Ga in the weakly bound state. The fractional area of the surface covered by weakly bound Ga is σ_{Ga} . The second assumption is that Ga desorption occurs only from this weakly bound state, which results in a Ga desorption term that is proportional to σ_{Ga} . We assume that for complete coverage ($Ga = 1$), the desorption flux is equal to the evaporation rate of Ga from liquid Ga as developed in ref. [55], and therefore we approximate the Ga desorption rate as $\sigma_{Ga} F_0(T_{sub})$, where $F_0(T_{sub})$ is the desorption flux of Ga vapor leaving liquid Ga. This assumption is consistent with the temperature dependence of the Ga desorption data as measured using DMS. This model does not require that Ga completely wet the GaN surface, since the shadowing effect of droplets could account for the observed behavior as well. In the limit of complete wetting, σ_{Ga} is the Ga surface coverage. Direct measurement of σ_{Ga} is complicated by a temperature gradient of $>20^\circ\text{C}$ across the substrate surface [55], and we have been unable to obtain a reliable measure of σ_{Ga} due to the strong temperature dependence of the coverage.

The DMS measurements shown in Figure 7 indicate that excess Ga reduces the growth rate. We assume that NH_3 reacts only with the strongly bound Ga, and that the excess Ga in the weakly bound sites reduces the growth rate by blocking the underlying reactive Ga sites. Further motivation for such a growth mechanism can be found in the work of Liu and Stevenson [78], who found that the coexistence of Ga and GaN enhanced the decomposition of NH_3 relative to Ga alone.

We let the growth rate be proportional to the fraction of strongly bound Ga sites that are exposed to the incident NH_3 , $(1-\sigma_{\text{Ga}})$. We now consider the following quantities:

$$\begin{aligned} F_N &= \text{total available incident N flux provided by the } \text{NH}_3 \\ F_{\text{Ga}} &= \text{total available Ga flux} \\ \sigma_{\text{Ga}} F_0(T_{\text{sub}}) &= \text{Ga desorption flux} \end{aligned}$$

where all temperature dependence will be included in the Ga desorption term, $\sigma_{\text{Ga}} F_0(T_{\text{sub}})$. DMS measurements of both the H_2 and Ga desorption fluxes show that the NH_3 reactivity does not depend on substrate temperature over the range (700°C - 820°C), and we therefore let F_N be independent of substrate temperature.

We wish to determine the steady-state growth rate when $F_{\text{Ga}} > F_N$. The time derivative of the Ga coverage is given by

$$(3) \quad \frac{1}{A} \frac{dN_{\text{Ga}}}{dt} = F_{\text{Ga}} - F_N(1 - \sigma_{\text{Ga}}) - \sigma_{\text{Ga}} F_0(T_{\text{sub}})$$

where the growth rate is $F_N(1 - \sigma_{\text{Ga}})$, and N_{Ga} is the number of Ga atoms on the surface. The substrate surface area is A . Solving equation (3) for σ_{G} at steady-state gives the growth rate

$$(4) \quad F_N(1 - \sigma_{\text{Ga}}) = F_N \left(\frac{F_{\text{Ga}} - F_N}{F_0(T_{\text{sub}}) - F_N} \right)$$

The results of this model are shown as solid lines in Fig. 42. As stated earlier, we estimate the desorption term $F_0(T_{\text{sub}})$ from the equilibrium vapor pressure of Ga over liquid Ga given in ref. [79]. We see from Fig. 42 that the measured data is in reasonable agreement with the steady-state solution given in equation (4). The only parameter used to fit the predictions of equation (4) to the measured data was F_N , which is equated to the known Ga flux for which H_2 is maximum.

The main points to be extracted from this discussion are that excess Ga reduces the formation rate of GaN, and that this effect can be minimized by increasing the substrate temperature. Additionally, we see that a drastic reduction in growth rate occurs when $F_{\text{Ga}} = F_0(T_{\text{sub}})$, where $\sigma_{\text{Ga}} = 1$ and growth is inhibited. We can also explain the increase in H_2 desorption observed after closing the Ga shutter as seen in Figure 5 as follows. During growth, excess Ga resides on the surface and reduces the growth rate by blocking the reactive GaN sites. After closing the Ga shutter, the excess Ga is depleted either by evaporation or by reaction with the GaN surface. As more surface area is exposed, the growth rate increases for a short time while the remaining surface Ga reacts with NH_3 on the exposed GaN surface.

9.4 Conclusions

Analysis of the transient H_2 and Ga desorption, along with the specular RHEED intensity show that Ga resides on the surface in both weakly bound and a strongly bound sites. After saturation of the strongly bound Ga sites, the Ga desorption flux increases, indicating the presence of the more weakly bound Ga. The adsorption process of Ga into the strongly bound sites produces H_2 as a byproduct.

Analysis of the steady-state growth rate using DMS shows that excess Ga reduces the growth rate. A rate equation giving the steady-state value of the Ga coverage in the weakly bound state was described. The key feature of this model is the blocking of reactive sites by the weakly bound Ga. The model shows that by increasing the substrate temperature, the growth rate can be increased due to reduced coverage of this excess Ga.

10 References

1. A. Piotrowska, A. Guivarc'h and G. Pelous, Solid State Electronics, **26**, 179 (1983)
2. C. J. Palmstrøm and D. V. Morgan, in *Gallium Arsenide Materials, Devices, and Circuits*, M. J. Howes and D. V. Morgan (eds.), (John Wiley & Sons Ltd., Chichester 1985), Vol. p. 195
3. T. Sands, V. G. Keramidas, A. J. Yu, K.-M. Yu, R. Gronsky and J. Washburn, J. Mater. Res., **2**, 262 (1987)
4. T. Sands, J. Metals, **38**, 31 (1986)
5. S. H. Chen, C. B. Carter, C. J. Palmstrøm and T. Ohashi, Mat. Res. Soc. Symp. Proc., **54**, 361 (1986)
6. T. Sands, V. G. Keramidas, J. Washburn and R. Gronsky, Appl. Phys. Lett., **48**, 402 (1986)
7. A. Lahav, M. Eizenberg and Y. Komem, J. Appl. Phys., **60**, 991 (1986)
8. S. H. Chen, C. B. Carter and C. J. Palmstrøm, J. Mater. Res., **3**, 1385 (1988)
9. R. Guérin and A. Guivarc'h, J. Appl. Phys., **66**, 2122 (1989)
10. X. Y. Zheng, J. C. Lin, D. Swenson, K. C. Hsieh and Y. A. Chang, Mater. Sci. Eng. B, **5**, 63 (1989)
11. D. B. Ingerly, D. Swenson, C.-H. Jan and Y. A. Chang, J. Appl. Phys., **80**, 543 (1996)
12. M. Ogawa, Thin Solid Films, **70**, 181 (1980)
13. A. Guivarc'h, R. Guérin, J. Caulet, A. Poudoulec and J. Fontenille, J. Appl. Phys., **66**, 2129 (1989)
14. T. Sands, Mater. Sci. and Engin. B, **1**, 289 (1989)
15. T. Sands, C. J. Palmstrøm, J. P. Harbison, V. G. Keramidas, N. Tabatabaie, T. L. Cheeks, R. Ramesh and Y. Silberberg, Mat. Sci. Rep., **5**, 99 (1990)
16. R. Guerin and A. Guivarc'h, J. Appl. Phys., **82**, 493 (1997)
17. D. B. Ingerly, D. Swenson, C. H. Jan and Y. A. Chang, J. Appl. Phys., **82**, 496 (1997)
18. T. Sands, E. D. Marshall and L. C. Wang, J. Mater. Res., **3**, 914 (1988)
19. L. C. Wang, B. Zhang, F. Fang, E. D. Marshall, S. S. Lau, T. Sands and T. Kuech, J. Mater. Res., **3**, 922 (1988)
20. T. Sands, J. P. Harbison, W. K. Chan, S. A. Schwarz, C. C. Chang, C. J. Palmstrøm and V. G. Keramidas, Appl. Phys. Lett., **52**, 1216 (1988)
21. C. H. Jan, D. Swenson, X. Y. Zheng, J. C. Lin and Y. A. Chang, Acta Metall. Mater., **39**, 303 (1991)
22. C. J. Palmstrøm, C. C. Chang, A. Yu, G. J. Galvin and J. W. Mayer, J. Appl. Phys., **62**, 3755 (1987)
23. S. M. Sze, *Physics of Semiconductor Devices*, Wiley, New York, (1971)
24. R. T. Tung, A. F. J. Levi, J. P. Sullivan and F. Schrey, Phys. Rev. Lett., **66**, 72 (1991)
25. E. H. Rhoderick and R. H. Williams, *Metal-Semiconductor Contacts*, Oxford University Press, Oxford, (1988)
26. J. R. Waldrop, J. Vac. Sci. Techn. B, **2**, 445 (1984)
27. J. R. Waldrop, Appl. Phys. Lett., **44**, 1002 (1984)
28. T. G. Finstad and J. S. Johannessen, Proceedings of the 10th Nordic Semiconductor Meeting, Elsinore, Denmark (1982)
29. H. F. Chuang, C. P. Lee and D. C. Liu, J. Electron. Mater., **24**, 767 (1995)
30. R. T. Tung, Appl. Phys. Lett., **58**, 2821 (1991)
31. T. J. Miller and M. I. Nathan, Appl. Phys. Lett., **61**, 2332 (1992)
32. S. M. Sze, *Physics of Semiconductor Devices*, (1985)

33. R. F. Schmitsdorf, T. U. Kampen and W. Monch, *Surface Science*, **324**, 249 (1995)
34. R. F. Schmitsdorf, T. U. Kampen and W. Monch, *J. Vac. Sci. Technol. B*, **15**, 1221 (1997)
35. T. Sands, C. J. Palmstrøm, J. P. Harbison, V. G. Keramidas, N. Tabatabaie, T. L. Cheeks, R. Ramesh and Y. Silberberg, *Mat. Sci. Rep.*, **5**, 99 (1990)
36. C. J. Palmstrøm and T. Sands, in *Contacts to Semiconductors: Fundamentals and Technology*, L. J. Brillson (ed.), (Noyes, Park Ridge, NJ 1993), Vol. p. 67
37. In *Binary Alloy Phase Diagrams*, T. B. Massalski (ed.), (1986)
38. P. Villars and L. D. Calvert, *Pearson's Handbook of Crystallographic Data for Intermetallic Phases*, American Society for Metals, (1985)
39. A. M. Wowchak, J. N. Kuznia and P. I. Cohen, *J. Vacuum Sci. Technol.*, **B7**, 733 (1989)
40. J. N. Kuznia, A. M. Wowchak and P. I. Cohen, *J. Elect. Mat.*, **19**, 561 (1990)
41. S. H. Liou, S. S. Malhotra, J. X. Shen, M. Hong, J. Kwo, H. S. Chen and J. P. Mannaerts, *J. Appl. Phys*, **73**, 6766 (1993)
42. M. Hong, H. S. Chen, J. Lwo, A. R. Kortan, J. P. Mannaerts, B. E. Weir and L. C. Feldman, *J. Crystal Growth*, **111**, 984 (1991)
43. B. T. Jonker, *J. Vacuum Sci. Technol.*, **8**, 3883 (1990)
44. A. M. Dabiran and P. I. Cohen, *J. Crystal Growth*, **150**, 23 (1995)
45. S. Nakamura, T. Mukai and M. Senoh, *Jpn J. Appl. Phys.*, **30**, L1998 (1991)
46. R. Gaska, A. Osinksy, J. W. Yang and M. S. Shur, *IEEE Electron Device Lett.*, **19**, 44 (1998)
47. Q. Chen, J. W. Yang, M. S. Shur and I. Adesida, *IEEE Electron Device Lett.*, **19**, 44 (1998)
48. A. C. Schmitz, A. T. Ping and A. Khan, *J. Electronic Mat.*, **27**, 255 (1998)
49. A. T. Ping, A. Khan and A. Adesida, *J. Electronic Mater.*, **25**, 819 (1996)
50. M. E. Lin, Z. Ma, F. Y. Huang and H. Morkoc, *Appl. Phys. Lett.*, **64**, 1003 (1994)
51. K. J. Duxstad, E. E. Haller and K. M. Yu, *J. Appl. Phys.*, **81**, 3134 (1997)
52. B. P. Luther, S. E. Mohney, J. M. Delucca and R. F. Karlicek, *J. Elect. Mat.*, **27**, 196 (1998)
53. R. Beresford, D. C. Paine and C. L. Briant, *J. Cryst. Growth*, **178**, 189 (1998)
54. R. Nowak and C. L. Li, *Thin Solid Films*, **305**, 297 (1997)
55. R. Held, D. E. Crawford, A. M. Johnston, A. M. Dabiran and P. I. Cohen, *J. Electronic Materials*, **26**, 272 (1997)
56. S. E. Mohney and X. Lin, *J. Electronic Materials*, **25**, 811 (1996)
57. C. J. Palmstrøm, N. Tabatabaie and S. J. Allen, Jr., *Appl. Phys. Lett.*, **53**, 2608 (1988)
58. C. J. Palmstrøm, B.-O. Fimland, T. Sands, K. C. Garrison and R. A. Bartynski, *J. Appl. Phys.*, **65**, 4753 (1989)
59. C. J. Palmstrøm, K. C. Garrison, S. Mounier, T. Sands, C. L. Schwartz, N. Tabatabaie, S. J. Allen, Jr., H. L. Gilchrist and P. F. Miceli, *J. Vac. Sci. Technol. B*, **7**, 747 (1989)
60. A. M. Wowchak, J. N. Kuznia and P. I. Cohen, *J. Vac. Sci. Technol. B*, **7**, 733 (1989)
61. C. J. Palmstrøm, S. Mounier, T. G. Finstad and P. F. Miceli, *Appl. Phys. Lett.*, **56**, 382 (1990)
62. C. J. Palmstrøm, T. L. Cheeks, H. L. Gilchrist, J. G. Zhu, C. B. Carter and R. E. Nahory, *Mat. Res. Soc. Extended Abstract*, **EA-21**, 63 (1990)
63. C. J. Palmstrøm, J. P. Harbison, T. Sands, R. Ramesh, T. G. Finstad, S. Mounier, J. G. Zhu, C. B. Carter, L. T. Florez and V. G. Keramidas, *Mat. Res. Soc. Symp. Proc.*, **198**, 153 (1990)
64. T. Sands, J. P. Harbison, R. Ramesh, C. J. Palmstrøm, L. T. Florez and V. G. Keramidas, *Mater. Sci. and Eng. B*, **6**, 147 (1990)

65. C. J. Palmstrøm, T. Sands, J. P. Harbison, T. G. Finstad, S. Mounier, L. T. Florez, V. G. Keramidas, J. G. Zhu and C. B. Carter, SPIE Proceedings, **1285**, 85 (1990)
66. C. J. Palmstrøm, T. L. Cheeks, H. L. Gilchrist, J.G. Zhu, C.B. Carter, B. J. Wilkens and R. Martin, J. Vac. Sci. Technol. A, **10**, 1946 (1992)
67. T. Sands, W. K. Chan, C. C. Chang, E. W. Chase and V. G. Keramidas, Appl. Phys. Lett., **52**, 1338 (1988)
68. M. Tanaka, M. Tsuda, T. Nishinaga and C. J. Palmstrøm, Appl. Phys. Lett., **68**, 84 (1996)
69. D. E. Brehmer, K. Zhang, C. J. Schwarz, S.-P. Chau, S. J. Allen, J. P. Ibbetson, J. P. Zhang, C. J. Palmstrøm and B. J. Wilkens, Appl. Phys. Lett., **67**, 1268 (1995)
70. D. E. Brehmer, Z. Kai, C. J. Schwarz, S. P. Chau, S. J. Allen, J. P. Ibbetson, J. P. Zhang, A. G. Petukhov, C. J. Palmstrøm and B. Wilkens, Solid-State Electron. , **40**, 241 (1996)
71. D. R. Schmidt, J. P. Ibbetson, D. E. Brehmer, C. J. Palmstrøm and S. J. Allen, Mat. Res. Soc. Symp. Proc., **475**, 251 (1997)
72. A. G. Petukhov, W. R. L. Lambrecht and B. Segall, Phys. Rev. B, **50**, 7800 (1994)
73. A. G. Petukhov, W. R. L. Lambrecht and B. Segall, Phys. Rev. B, **53**, 3646 (1996)
74. S. Strite and H. Morkoc, J. Vacuum Sci. Technol, **B10**, 1237 (1992)
75. N. E. Lee, R. C. Powell, Y.-W. Kim and J. E. Greene, J. Vacuum Sci. Technnol. A, **13**, 2293 (1995)
76. C. R. Jones, T. Lei, R. Kaspi and K. R. Evans, Unpublished., (1995)
77. N. Newman, J. Ross and M. Rubin, Appl. Phys. Lett., **62**, 1242 (1993)
78. S. S. Liu and D. A. Stevenson, J. Electrochem. Soc., **125**, 1161 (1978)
79. In *CRC Handbook of Chemistry and Physics*, D. R. Lide (ed.), CRC Press, Boca Raton (1990)

AIR FORCE OFFICE OF SCIENTIFIC
RESEARCH (AFOSR)
NOTICE OF TRANSMITTAL TO DTIC. THIS
TECHNICAL REPORT HAS BEEN REVIEWED
AND IS APPROVED FOR PUBLIC RELEASE
IWA AFR 190-12. DISTRIBUTION IS
UNLIMITED.
YONNE MASON
STINFO PROGRAM MANAGER